



Article

<https://doi.org/10.1038/s41558-025-02276-3>

Worldwide rooftop photovoltaic electricity generation may mitigate global warming

Received: 20 March 2024

Accepted: 6 February 2025

Published online: 07 March 2025

Check for updates

Zhixin Zhang ^{1,2,3,31}, Zhen Qian ^{1,2,4,31}, Min Chen ^{1,5,6}✉, Rui Zhu ⁷, Fan Zhang ⁸, Teng Zhong ¹, Jian Lin ¹, Liang Ning ¹, Wei Xie ¹, Felix Creutzig ^{2,3,9}, Wenjun Tang ¹⁰, Laibao Liu ^{11,12}, Jiachuan Yang ¹³, Ye Pu ¹⁴, Wenjia Cai ¹⁵, Yingxia Pu ^{5,16,17}, Deer Liu ¹⁸, Hui Yang ¹⁹, Hongjun Su ²⁰, Mingyue Lu ²¹, Fei Li ²², Xufeng Cui ²³, Zhiwei Xie ²⁴, Tianyu Sheng ¹, Kai Zhang ¹, Paolo Santi ^{25,26}, Lixin Tian ^{27,28}, Guonian Lü ^{1,5} & Jinyue Yan ^{29,30}

Rooftop photovoltaic (RPV) is often understood as a niche contribution to climate change mitigation. However, the global potential of RPVs to mitigate global warming is unknown. Here we map the global rooftop area at 1-km resolution, quantifying 286,393 km² of rooftops worldwide through geospatial data mining and artificial intelligence techniques. Using nine advanced Earth system models from the coupled model intercomparison project phase 6, we reveal that RPVs could substantially contribute to reducing global temperatures by 0.05–0.13 °C before 2050. Region-specific analysis underscores the variability in RPV potential and the necessity of tailored approaches to optimize RPV deployment, considering local solar resources, existing infrastructure and grid carbon intensity. Our findings reveal that leveraging RPV systems offers a viable and impactful strategy for reducing carbon footprints and combating climate change globally, while advocating targeted interventions to enhance the benefits of RPVs, particularly in areas with high solar radiation or rapid urbanization.

Global warming, driven by carbon emissions mainly from fossil fuels, has caused a 1.07 °C rise in global surface temperature during the 2010s compared with the pre-industrial era¹. This warming poses substantial climate challenges to natural systems and human societies². The 2015 Paris Agreement underscores the importance of limiting global temperature rise to below 1.5 °C or 2 °C (ref. 3). However, without intervention, the global temperature is projected to rise by 2.8 °C by the end of the century, pushing the Earth system closer to or surpassing the climate tipping points⁴.

Solar energy is an essential technology for climate change mitigation, showing impressive technological learning curves and large future potential^{5,6}. While often underestimated in climate stabilization models, it could provide the single largest contribution to mitigation in 2050⁷. Rooftop photovoltaic (RPV), initially a niche solution⁸, may also offer a global-scale opportunity to reduce fossil fuel reliance⁹. Previous studies have shown that the carbon mitigation potential of

RPVs in China is up to 4 gigatonnes (Gt), accounting for 70% of the country's emissions from the electricity and heat sector¹⁰. However, at the global level, studies have mainly focused on the technical benefits and economic feasibility of RPVs^{9,11}. Analyses of the impact of RPVs on carbon mitigation and, consequently, their benefits to global climate, particularly in regions with diverse natural and societal conditions, are notably absent. Bridging this gap is vital for understanding the role of RPVs in climate change mitigation and guiding effective energy policy-making.

Evaluating the potential of RPVs over large geographic areas faces a considerable challenge in obtaining a comprehensive, high-quality global distribution of the rooftop area. Existing datasets, derived from on-site surveys or high-resolution Earth observations, are region-specific and have heterogeneous spatiotemporal references, leading to inconsistencies and variabilities in coverage and quality when applied globally^{12–14}. Global rooftop area estimates also suffer from uncertainties due to the

A full list of affiliations appears at the end of the paper. ✉ e-mail: chenmin0902@njnu.edu.cn

limitations of conventional remote sensing technologies with moderate resolutions in the tens to hundreds of metres. This could lead to misidentification of dispersed and fine-scale building rooftops, introducing cumulative errors in rooftop area quantifications^{15,16}. The limited understanding of fine-grained global rooftop area hinders accurate assessments of RPV potential and their spatial variations^{17,18}.

In this study we integrate geospatial data mining and artificial intelligence techniques to estimate the global rooftop area at a resolution of 1 km, addressing the lack of detailed geographic distributions. We evaluate the technical potential of RPVs, focusing on regional differences. Technical potential quantifies electricity generation based on resource availability, system performance and physical availability for RPV development¹⁹. This metric provides a baseline for understanding maximum feasible deployment under theoretical conditions, serving as a foundation for further studies on economic or market viability. For the associated environmental and climate benefits, this study estimates carbon mitigation from substituting grid electricity with RPVs using a baseline emission methodology. Then, by using nine advanced Earth system models (ESMs) from coupled model intercomparison project phase 6 (CMIP6), we explore the potential warming mitigation achievable by mid-century under various future climate policy scenarios. We also examine the spatial distribution of this potential, particularly in climate-sensitive regions and its role in mitigating climate tipping risks. These analyses enhance understanding of impact of regional RPVs on global energy landscapes and highlight how resource endowments shape their climate mitigation contributions.

Global rooftop area estimation

We developed a two-stage approach, combining both top-down and bottom-up methods, to estimate the global rooftop area (Extended Data Fig. 1). In the top-down stage, a deep learning model based on the Vision Transformer architecture¹⁹ (Methods) was trained and applied to high-resolution (1.2 m) remote sensing imagery to quantify rooftop area in selected representative regions. In the bottom-up stage, we modelled the nonlinear relationship between the rooftop area determined in the top-down stage and various geospatial variables using an ensemble of random forests. This allowed for the global extrapolation of rooftop area estimates.

The deep learning model was initially pretrained on publicly available benchmark datasets covering ~2,500 km² (Methods and Supplementary Table 1). This pretraining phase enabled the model to recognize common building patterns across imagery with varying spatial resolutions, architectural styles and geographic contexts²⁰. The model was then fine-tuned using manually labelled high-resolution remote sensing imagery, which covered 1,600 km² of diverse landscapes worldwide (Methods and Extended Data Fig. 2a), including 835,253 labelled buildings. The deep learning model was evaluated on a separate set of high-resolution remote sensing images covering 386 km² from various locations, ensuring that these images were not part of the training process or model optimization (Methods and Extended Data Fig. 2b). The validation results confirmed that the model can accurately quantify rooftop area across a variety of landscapes globally (Methods and Extended Data Fig. 3).

In the bottom-up stage, we partitioned the global land surface into discrete spatial grids, each consisting of 1 km² units. Geospatial datasets were aggregated into these grids, including population statistics, night-time light imagery, road networks, digital elevation models and land use and land cover data (Methods and Supplementary Table 2). An ensemble of random forest models was then used to estimate the global rooftop area from these datasets. To develop the predictive models, 1,724 cities were strategically selected as regions of interest (here the term ‘city’ refers to administrative divisions that may include both rural and urban areas; Extended Data Fig. 4). The trained deep learning model was applied to quantify rooftop area in these regions. Subsequently, 8.5 million spatial grid samples were generated, with

rooftop area as the dependent variable and the aforementioned geospatial datasets as independent variables, which were then used to train the predictive models (Methods).

The extrapolated global rooftop area was assessed using 16,000 grids across macroregions (Methods and Extended Data Figs. 5, 6 and 7 and Supplementary Fig. 3). The grid-level analysis showed high consistency across regions ($r^2 = 0.89$; bias error = 2%). Additionally, the global estimates demonstrated high consistency with other reference datasets, including the Google building footprints (GBF)²¹, the Microsoft building footprints (MBF)²², the global human settlement layer (GHSL)²³ and the world settlement footprint 3D (WSF3D)²⁴, with r^2 values ranging from 0.75 to 0.85 (Methods and Extended Data Fig. 8). The global rooftop area was estimated to be 286,393 km², with 30% of the total area contributed by East Asia (E-ASI) and 12% by North America (N-AME). At the national level, China (74,426 km²) and the United States (30,928 km²) ranked first and second, respectively, followed by India (23,087 km²) in third place (Fig. 1a). These global rooftop area estimates provide comprehensive coverage, accurately capturing the morphology of urban agglomerations in both developing and developed regions (Fig. 1b–d).

Electricity generation and carbon mitigation

Owing to geographical constraints such as rooftop orientation, slope and shading between buildings, only a fraction of rooftops is suitable for RPV installation. We calculated available rooftop area using a scaling factor of 30% based on general cases reported (Supplementary Table 3). Solar energy input was derived from a high-resolution global surface solar radiation dataset (3-h temporal, 10-km spatial resolution)²⁵. The dataset, derived from ISCCP and ERA5 datasets using improved physical inversion algorithms, has demonstrated better accuracy than GEWEX SRC, CERES and ISCCP datasets²⁵. For regional studies, higher-quality datasets such as NRSDB, CAMS or CM-SAF are recommended, although they currently lack global coverage²⁶. The electricity generation potential of an RPV system was defined as the maximum achievable electricity production for a given rooftop area. By considering a 20% panel conversion efficiency and an 80% overall efficiency, the conversion from solar energy to electricity generation can be accomplished (Methods). The carbon mitigation potential was defined as the CO₂ reduction from replacing grid electricity with RPV electricity and thus calculated using baseline grid emission factors developed by the technical working group of the international financial institutions (Methods). To explain the variations in the main results caused by different panel efficiencies and rooftop availability, we conducted sensitivity evaluations (Supplementary Tables 4–6).

Solar radiation intensity largely determines the electricity generation of RPVs. The global average surface solar radiation is ~1,500 kWh m⁻² yr⁻¹, with hotspots concentrated in Africa (2,000–2,200 kWh m⁻² yr⁻¹). However, owing to limited building stock, the installation potential in Africa (1,188 GW) is only 7% of the global total. In contrast, the macroregions (N-AME, Northern America; N-EUR, Northern Europe; W-EUR, Western Europe and E-EUR, Eastern Europe) with lower solar radiation (900–1,200 kWh m⁻²) have an installation potential of 4,339 GW, which constitutes 25% of the world’s total (Extended Data Fig. 9a,b). National disparities between installed capacity and solar resources are evidenced by the volume and intensity of electricity generation (Fig. 2a). More countries (62%) have advantages (in the top 50%) in only one aspect of volume or intensity.

The carbon mitigation benefits of RPVs depend on grid baseline carbon intensity. While the global average carbon intensity stands at 529 gCO₂ kWh⁻¹, national values range from 0 to 1,330 gCO₂ kWh⁻¹ (Extended Data Fig. 9c). Macroregions with higher clean energy shares, such as W-EUR, generally exhibit carbon intensities below the average (206 gCO₂ kWh⁻¹), while fossil fuel-reliant regions such as E-ASI exceed the average (700 gCO₂ kWh⁻¹). Spatial disparities in installed capacity and grid intensity are reflected in mitigation volume and intensity (Fig. 2b). Countries with advantages (in the top 50%) in both mitigation

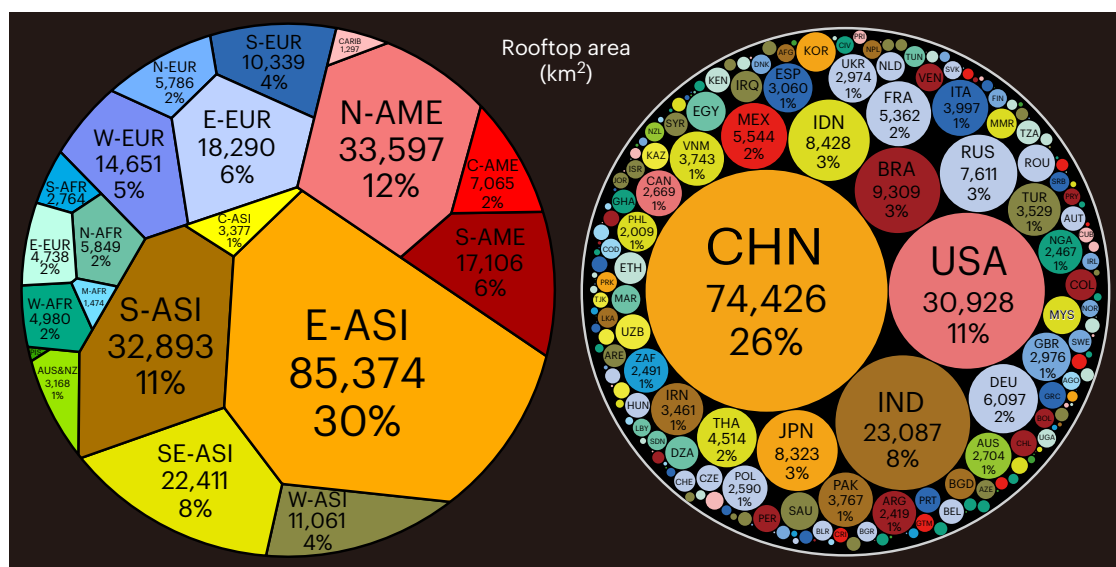
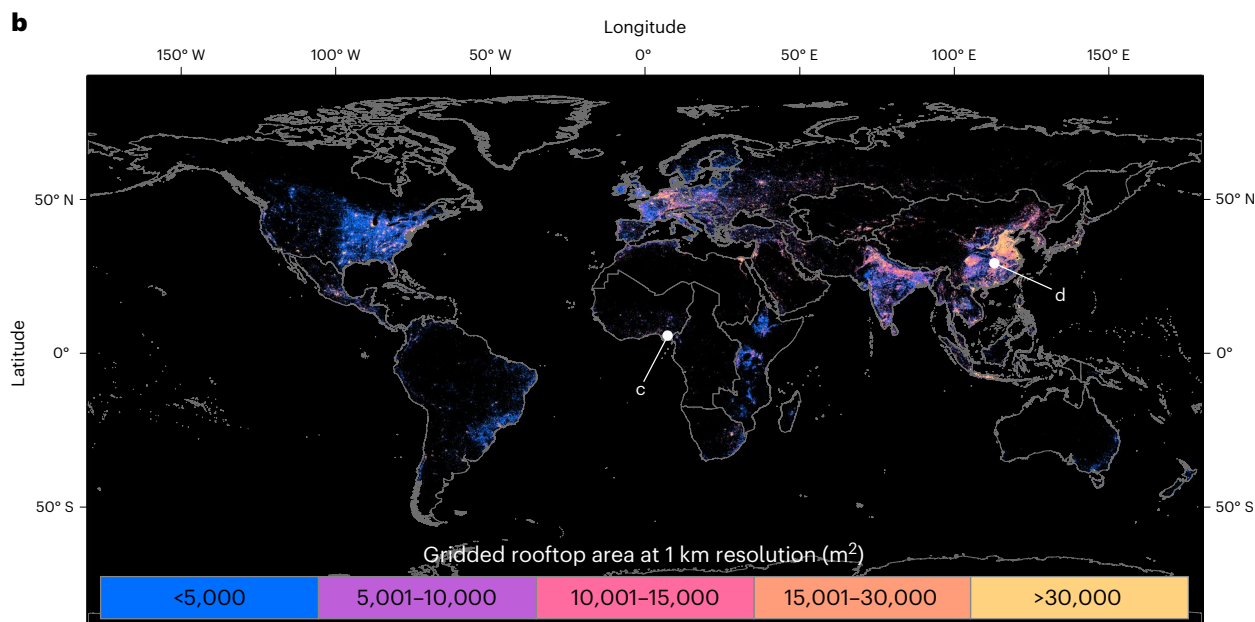
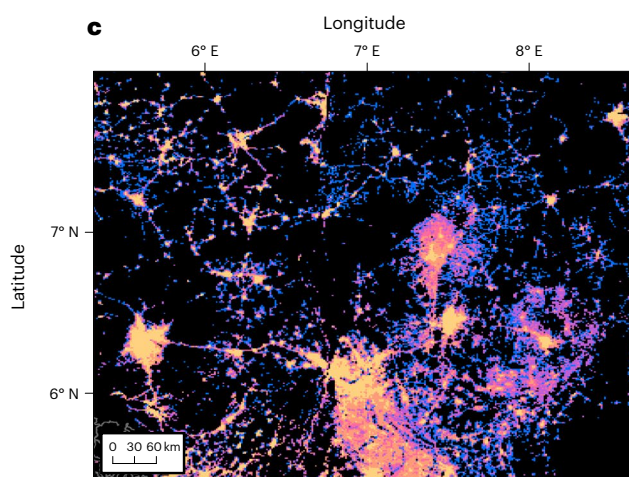
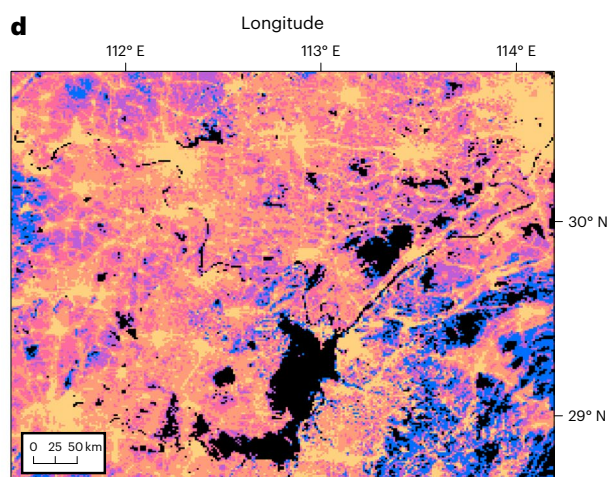
a**b****c****d**

Fig. 1 | Global rooftop area distribution. **a**, Rooftop area (in km^2) at the macroregional and national scales. **b**, Global spatial distribution on a 1-km grid. **c,d**, Close-up of specific regions (indicated in **b**), covering approximately 1 and 0.7 million km^2 in Nigeria (**c**) and China (**d**). Supplementary Fig. 3 contains the definitions and abbreviations for the macro-regions and countries.

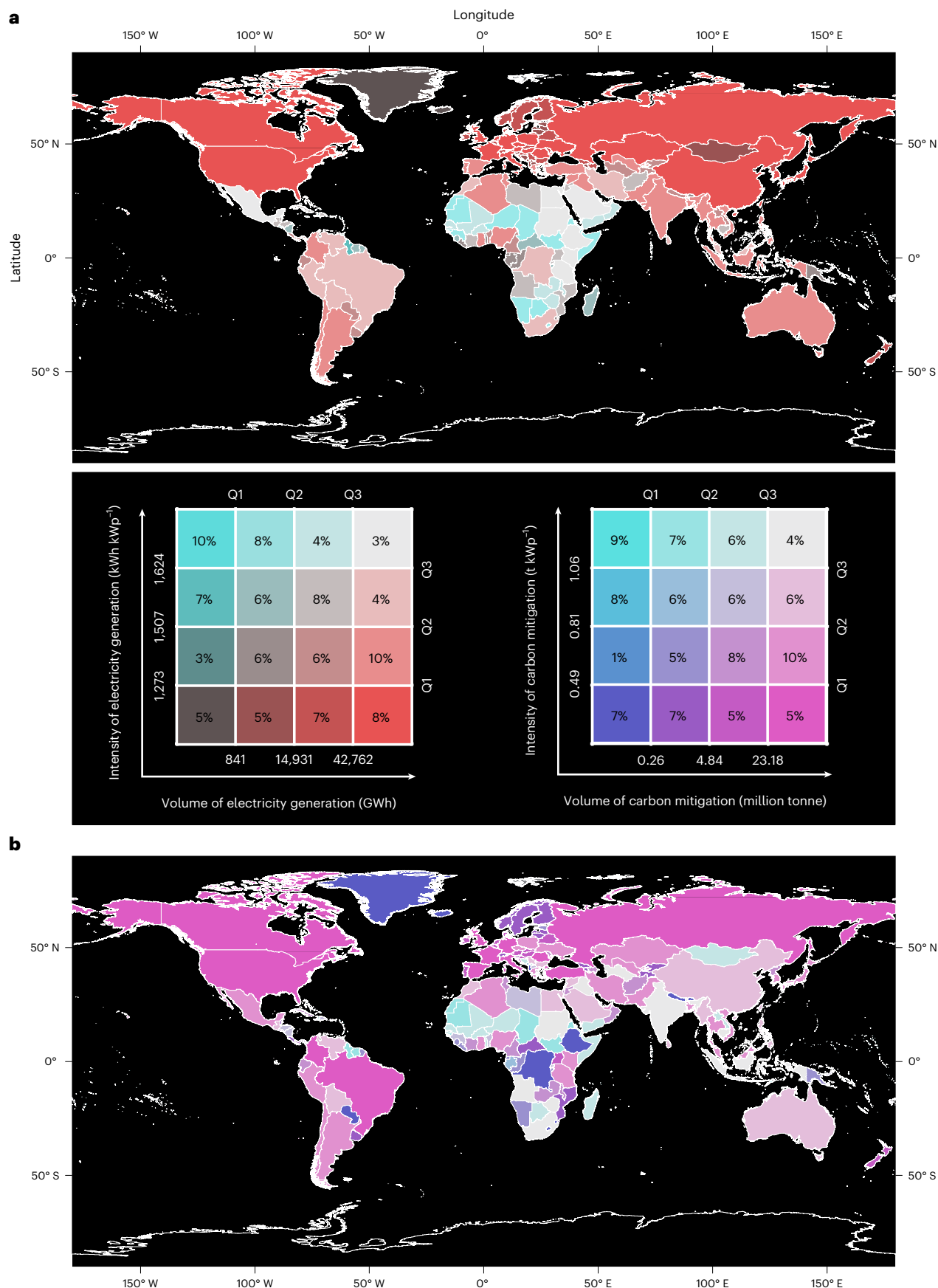


Fig. 2 | Global distribution of RPV electricity generation and carbon mitigation potential. **a,b**, Electricity generation (**a**) and carbon emission reduction (**b**). Intensity and volume combinations are divided by quartiles, with the percentages

of countries in each combination summarized. While the volume index refers to the benefits provided by all potential RPV installations, the intensity index indicates the benefits provided per unit of potential RPV installation.

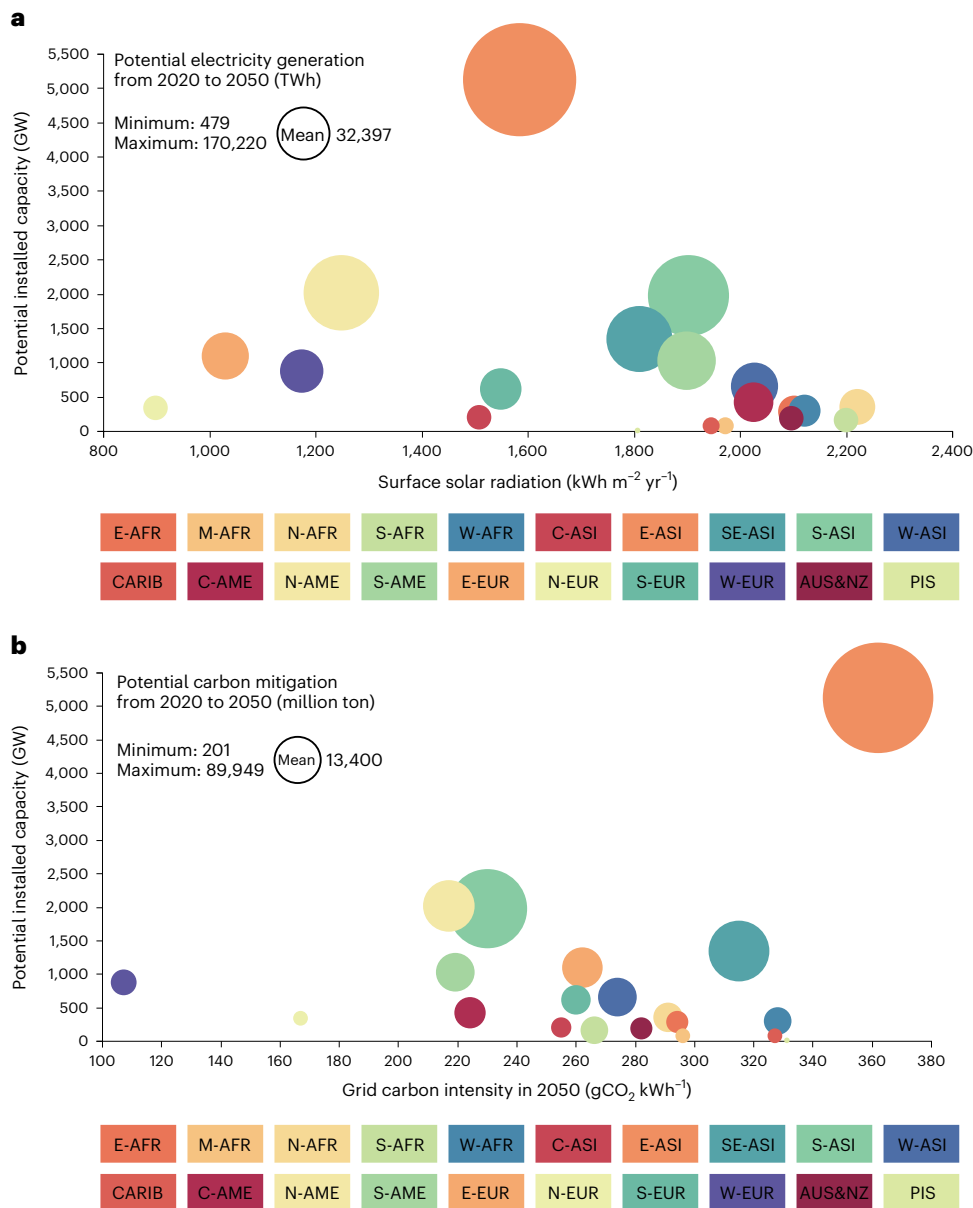


Fig. 3 | Cumulative potential from 2020 to 2050 in the STEPS scenario. **a,b,** Electricity generation (**a**) and carbon mitigation (**b**) for different macroregions are shown as bubbles of different sizes. The indicators of installed capacity, solar radiation and grid carbon intensity explain the reasons behind regional differences.

volume and intensity accounted for 22% of the total. Notably, 9% of the countries, including Egypt, Sudan, South Africa and many other African, Asian and American countries, achieved dual volume-intensity benefits in both electricity generation and carbon mitigation.

While global RPV currently offers substantial carbon mitigation potential, ongoing energy transitions are gradually lowering grid carbon intensity. Scenarios—stated policies (STEPS), sustainable development (SDS) and net-zero emission (NZE)—represent different visions for energy transition and climate goals (Supplementary Note 1). Each outlines varying levels of constraints, where the increasing penetration of clean energy and optimization of power technologies progressively reduce the carbon mitigation potential of RPVs. From 2020 to 2050, the grid carbon intensity is expected to decrease by 48%, 96% and 101%, respectively, under the three scenarios (Supplementary Note 2 and Supplementary Fig. 4). Correspondingly, RPV electricity generation contributes to cumulative global carbon mitigation of 268, 144 and 102 Gt over three decades, respectively (Supplementary Fig. 5). At the macroregional level, different resource endowments in terms of installed potential, solar radiation

and grid carbon intensity remain key factors driving differences in RPV electricity generation and carbon mitigation potential (Fig. 3).

Mitigations of global warming and climate tipping point risk

The conversion from RPV carbon mitigation to global warming mitigation potential was performed using the transient climate response to cumulative emissions of CO_2 (TCRE)²⁷, a well-established metric that quantifies the linear relationship between cumulative carbon emissions and global temperature. Regional temperatures also exhibit a linear response to cumulative carbon emissions²⁷. We calculated regional TCRE (RTCRE) by aggregating data from nine ESMs (Methods). By applying this method, we were able to translate the carbon mitigation potential of RPVs into an estimated global and regional warming mitigation. The spatial pattern of RTCRE values varied across different latitudes and elevations (Extended Data Fig. 10a). The RTCRE values on land range from 0.7 to 6.9 °C per trillion tonnes of carbon (TtC), with an average of 2.4 ± 0.8 °C per TtC. The highest values were observed for

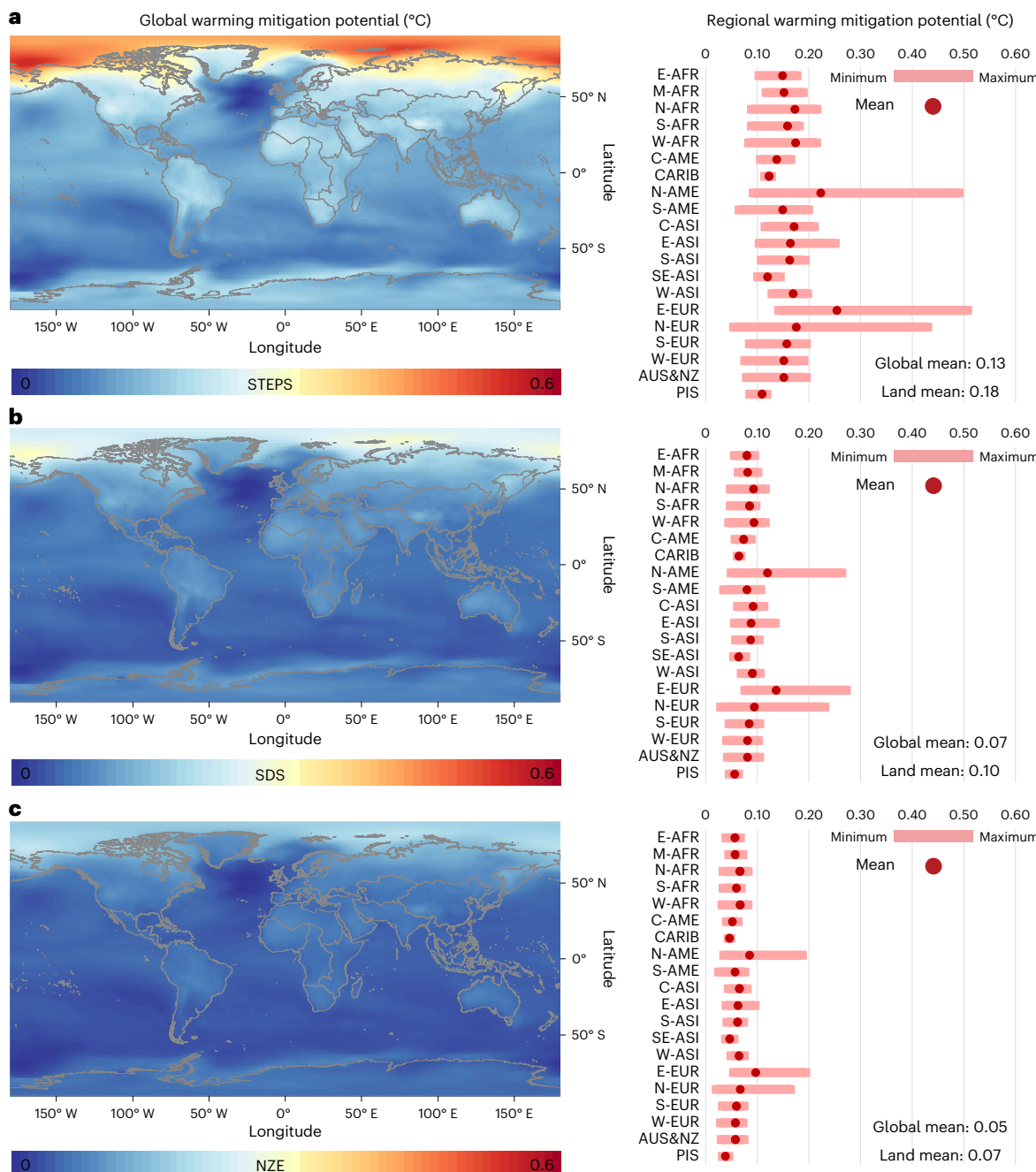


Fig. 4 | Cumulative global warming mitigation potential from 2020 to 2050 under different scenarios. a–c, STEPS (a), SDS (b) and NZE (c). Macroregional statistics show that regions (E-EUR and N-AME) close to the Arctic are more sensitive to global climate change and these regions are expected to benefit more from global RPV carbon mitigation efforts.

high-latitude E-EUR and N-AME ($>3^{\circ}\text{C TtC}^{-1}$). Additionally, high-altitude regions such as the Qinghai-Tibet Plateau and the Western Australian Plateau in mid-to-low latitudes also have relatively high RTCRE ($2.5\text{--}3.5^{\circ}\text{C TtC}^{-1}$). The spatial pattern of the intermodel distribution of RTCRE (Extended Data Fig. 10b, calculated as the standard deviation among the models) indicated that RTCRE uncertainty was generally higher in high-latitude regions than in mid- to low-latitude regions in the Northern Hemisphere.

In total, GHG emission reduction through RPVs from 2020 to 2050 under the STEPS, SDS and NZE scenarios are projected to mitigate global warming by $0.13\text{--}0.05^{\circ}\text{C}$ (Fig. 4). Since the global average temperature has already risen by 1.2°C above pre-industrial levels by 2020³, meeting the goals of the 1.5 or 2°C warming limit requires an

additional margin of only 0.3 or 0.8°C . Under the STEPS scenario, we find that if RPV potential is not tapped, the additional carbon emissions from the power grid from 2020 to 2050 could lead to an approximate increase of 0.13°C in global temperature. This equals 43% and 16% of the remaining allowable warming below the 1.5 and 2.0°C thresholds (0.3 and 0.8°C), respectively. However, more stringent climate policies (SDS and NZE scenarios) will optimize the power mix and further mitigate its baseline carbon emissions, resulting in greater mitigation of the relative avoidable global warming (0.07 and 0.05°C). These contribute an additional $17\text{--}23\%$ and $6\text{--}9\%$ to meet the 1.5 or 2.0°C thresholds, respectively.

The contributions of RPVs to global warming mitigation may be particularly substantial in regions with high climate sensitivity,

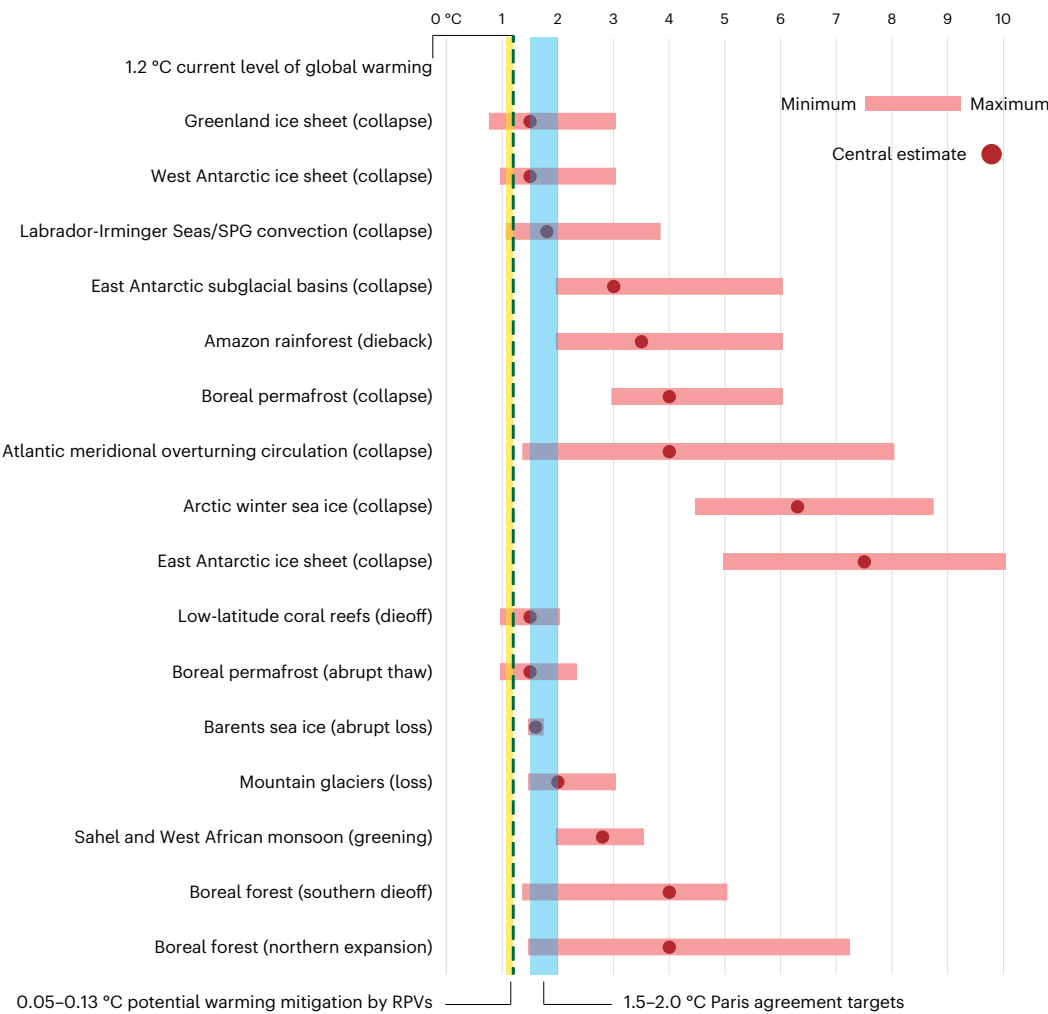


Fig. 5 | Potential climate impacts of RPVs on climate-sensitive areas. The estimation of temperature thresholds for tipping points of climate-sensitive areas is revised from ref. 29. The 1.5–2 °C temperature target is indicated by the blue range. The potential warming mitigation derived from RPV relative to the current warming level (green dashed line) is shown in the yellow range.

where irreversible impacts on society and ecosystems are likely to occur once tipping points are reached²⁸. Currently, at the warming level of ~1.2 °C, five tipping points have already been approached, with an additional five expected to be reached when the 1.5 °C warming is achieved²⁹. In this context, efforts of RPV carbon mitigation are expected to reduce the likelihood of triggering these climate-critical thresholds. For example, RPVs may potentially provide a 25–66% additional warming margin to reach the lower warming threshold for the Atlantic meridional overturning circulation collapse (Fig. 5). RPVs could also potentially contribute an additional 17–44% margin for reaching the lower threshold for Barents Sea ice abrupt loss and mountain glaciers loss.

Discussion

Although previous studies demonstrated substantial electricity generation and carbon mitigation benefits of RPVs in energy transition, further investigation is required to understand their role in addressing climate change challenges. Here we estimated global rooftop areas at 1-km resolution by using geospatial data mining and artificial intelligence techniques, addressing the critical bottleneck in detailed energy assessments. Furthermore, we systematically assessed the climatic benefits of global RPV electricity generation, highlighting its potential contribution to climate change mitigation, particularly towards achieving global temperature targets.

Using nine advanced ESMs from CMIP6, we fill a critical gap in evaluating the climatic benefits of RPVs. From 2020 to 2050, potential carbon mitigation from RPVs corresponds to a global warming mitigation of 0.05–0.13 °C. This provides an additional 17–43% margin towards the 1.5 °C warming threshold and reduces risks of triggering the tipping points in climate-sensitive regions. High-resolution global rooftop area estimation further supports detailed energy assessments. Policy-makers often face trade-offs between coverage and resolution, but our robust and scalable method enables accurate large-scale assessments. Specifically, the top-down approach, which applies a deep learning model on high-resolution remote sensing imagery to quantify rooftop areas in selected regions, reduces bias errors and cumulative inaccuracies from medium-to-low resolution imagery or crowdsourced geographic information^{9,30}. The bottom-up method enables efficient extrapolation of global rooftop area, ensuring accurate and seamless predictions. While this study successfully estimated the global rooftop area distribution at high resolution, accuracy was constrained by uncertainties in explanatory variables and geographical heterogeneity, causing regional variations in our data quality. Future work could refine region-specific variables, introduce spatiotemporal causal reasoning and integrate domain-specific knowledge to improve the estimations. The detailed global baseline data and potential distribution simulations provided may offer valuable micro-level support for future macro-level climate change integrated assessment models.

or energy system models^{31,32}. This could enhance their decision-making capabilities at regional and city levels, promoting more precise energy planning and climate policy evaluation.

Encouraging citizen participation in energy production and turning them into consumers of the energy they produce are crucial steps in tackling global climate challenges³³. Our results show considerable global potential for widespread RPV deployment. However, future sustainable development should not rely solely on universal solutions. Our results highlight the necessity for regional planning that adapts to local conditions to enhance the energy and climate benefits of RPVs. Considering volume and intensity metrics and perspectives of electricity generation and carbon mitigation, we delineate advantageous combinations for developing RPVs in different regions, advocating for the rational use of resource endowments. For instance, despite holding 60% of the best solar resources globally, Africa accounts for only 1% of photovoltaic (PV) installations. Poor energy services and reliance on polluting energy sources further impede the progress of Africa in addressing environmental degradation and climate change³⁴. Our results suggest that RPV development could provide substantial energy and environmental benefits in most African countries, serving as a key driver of sustainable development. Additionally, our results indicate the most influential regions and those most likely to benefit from the global effort of broad deployment of RPVs. For example, in developing countries with large populations such as China and India, the widespread adoption of RPVs not only facilitates their own energy transition, but also plays a pivotal role in assisting other regions around the globe to combat climate change, especially in regions with high latitudes and altitudes or those approaching their tipping points.

The main results of this study focus on the technical potential of RPVs and their associated environmental and climate benefits. We adopted theoretical assumptions to provide clear and quantifiable references. We also documented comparisons of our main results with selected studies at global, regional, national and municipal levels, with details provided in Supplementary Table 7. Under the same assumptions, at the global level, our estimated annual electricity generation potential of 19,483 TWh is comparable to the 18,040 TWh estimated by ref. 35. For Switzerland, our estimated rooftop area of 320 km² is similar to the 267 ± 71 km² estimated by ref. 36. For states and counties in the United States, our results on rooftop area, electricity generation and carbon mitigation are comparable to those reported by Google Project Sunroof³⁷. These comparisons with high-resolution, top-down studies demonstrate the high accuracy of our main results, falling within the range of estimates reported in the current literature.

For global-scale assessments, we used simplified methods with globally uniform assumptions to account for complex external factors. The impacts of varying rooftop availability and PV panel efficiency on the main results are presented in Supplementary Tables 4–6. We suggest that future research investigate local benchmarks when targeting various deployment scenarios. Specifically, rising temperatures affect the actual efficiency of PV panels and this effect is material-dependent (Supplementary Table 8)³⁸. Panel materials with smaller band gaps are generally more sensitive to temperature and moisture in the atmosphere³⁹. Furthermore, based on IPCC global warming scenarios, by 2100, the energy output of silicon PV could decrease by 15 kWh kWP⁻¹, with some regions experiencing losses of up to 50 kWh kWP⁻¹ (ref. 40). Additionally, compared with horizontal installation assumed in this study, installations with optimal tilt angles, single-axis vertical tracking, single-axis horizontal tracking and dual-axis tracking could increase the final radiation received by approximately 1.19, 1.22, 1.35 and 1.39 times, respectively⁴¹. Globally, as latitude increases, the advantages of tilted and tracking systems over horizontal installations also become more pronounced⁴¹. Our study provides a starting point for large-scale assessments of RPV potential, which can be expanded in future studies by incorporating meteorological simulation and urban morphology. This would enhance regional applicability and support

the development of optimal PV deployment strategies in complex urban environments.

Our assessment of the theoretical potential of RPVs highlights their substantial climate mitigation benefits. However, realizing this potential within the existing energy infrastructure involves complex factors. Achieving high PV scenarios requires policies supporting PV technological innovation and coordinated plans to accommodate large-scale PV power generation. This involves modernizing power market regulations, expanding transmission grids and scaling up storage technologies, all while addressing issues related to supply and demand balance^{42,43}. In addition, peer effects have been recognized as important motivators for installations, as they are critical in influencing climate-related decision-making through geographic effects and social network effects⁴⁴. To most effectively expand the use of solar panels, policy-makers can increase cumulative use by deploying them in areas where they are sparse, thus taking advantage of the proximity effect⁴⁵. Moreover, through a combination of government interventions and adaptive business models, racial inclusiveness of PV can be effectively realized and the penetration of PV in all communities may be facilitated⁴⁶.

In summary, our study not only proves the immense potential of RPVs in promoting sustainable energy solutions but also suggests that fully exploiting their potential can hasten the transition to a more climate-resilient world. Although unlocking this potential still requires policy-makers and society to overcome future organizational and financial challenges, it is expected that RPVs will provide effective clean energy solutions in many regions afterwards. Our quantification of the substantial climate benefits of RPVs will motivate energy planners to capitalize on this opportunity, while also encouraging researchers to further explore the potential of other forms of building-integrated PVs that seamlessly integrate energy production with urban infrastructure, thereby expanding the scope and impact of renewable energy applications.

Online content

Any methods, additional references, Nature Portfolio reporting summaries, source data, extended data, supplementary information, acknowledgements, peer review information; details of author contributions and competing interests; and statements of data and code availability are available at <https://doi.org/10.1038/s41558-025-02276-3>.

References

1. IPCC: Summary for Policymakers. In *Climate Change 2021: The Physical Science Basis* (eds Masson-Delmotte, V. et al.) (Cambridge Univ. Press, 2021).
2. Mora, C. et al. Broad threat to humanity from cumulative climate hazards intensified by greenhouse gas emissions. *Nat. Clim. Change* **8**, 1062–1071 (2018).
3. IPCC Special Report on Global Warming of 1.5 °C (eds Masson-Delmotte, V. et al.) (WMO, 2018).
4. Emissions Gap Report 2022: The Closing Window—Climate Crisis Calls for Rapid Transformation of Societies (UNEP, 2022).
5. Victoria, M. et al. Solar photovoltaics is ready to power a sustainable future. *Joule* **5**, 1041–1056 (2021).
6. Ram, M. et al. Global energy transition to 100% renewables by 2050: not fiction, but much needed impetus for developing economies to leapfrog into a sustainable future. *Energy* **246**, 123419 (2022).
7. Creutzig, F., Hilaire, J., Nemet, G., Müller-Hansen, F. & Minx, J. C. Technological innovation enables low cost climate change mitigation. *Energy Res. Soc. Sci.* **105**, 103276 (2023).
8. Nemet, G. F. *How Solar Energy Became Cheap: A Model for Low-Carbon Innovation* (Routledge, 2019).
9. Joshi, S. et al. High resolution global spatiotemporal assessment of rooftop solar photovoltaics potential for renewable electricity generation. *Nat. Commun.* **12**, 5738 (2021).

10. Zhang, Z. et al. Carbon mitigation potential afforded by rooftop photovoltaic in China. *Nat. Commun.* **14**, 2347 (2023).
11. Yan, J., Yang, Y., Elia Campana, P. & He, J. City-level analysis of subsidy-free solar photovoltaic electricity price, profits and grid parity in China. *Nat. Energy* **4**, 709–717 (2019).
12. Brovelli, M. A. & Zamboni, G. A new method for the assessment of spatial accuracy and completeness of OpenStreetMap building footprints. *ISPRS Int. J. Geo-Inf.* **7**, 289 (2018).
13. Zhang, Z. et al. Vectorized rooftop area data for 90 cities in China. *Sci. Data* **9**, 66 (2022).
14. Milojevic-Dupont, N. et al. EUBUCO v0.1: European building stock characteristics in a common and open database for 200+ million individual buildings. *Sci. Data* **10**, 147 (2023).
15. Esch, T. et al. Breaking new ground in mapping human settlements from space—the global urban footprint. *ISPRS J. Photogramm. Remote Sens.* **134**, 30–42 (2017).
16. Marconcini, M. et al. Outlining where humans live, the world settlement footprint 2015. *Sci. Data* **7**, 242 (2020).
17. Castellanos, S., Sunter, D. A. & Kammen, D. M. Rooftop solar photovoltaic potential in cities: how scalable are assessment approaches? *Environ. Res. Lett.* **12**, 125005 (2017).
18. Gassar, A. A. A. & Cha, S. H. Review of geographic information systems-based rooftop solar photovoltaic potential estimation approaches at urban scales. *Appl. Energy* **291**, 116817 (2021).
19. Gagnon, P., Margolis, R., Melius, J., Phillips, C. & Elmore, R. *Rooftop Solar Photovoltaic Technical Potential in the United States: A Detailed Assessment* (NREL, 2016).
20. Ma, Y., Chen, S., Ermon, S. & Lobell, D. B. Transfer learning in environmental remote sensing. *Remote Sens. Environ.* **301**, 113924 (2024).
21. Sirko, W. et al. Continental-scale building detection from high resolution satellite imagery. Preprint at <https://arxiv.org/abs/2107.12283> (2021).
22. Bing Maps Team. Microsoft building footprints. GitHub <https://github.com/microsoft/GlobalMLBuildingFootprints> (2024).
23. Pesaresi, M. & Politis, P. *GHS-BUILT-S R2023A—GHS Built-up Surface Grid, Derived From Sentinel2 Composite and Landsat, Multitemporal (1975–2030)* (European Commission, Joint Research Centre (2023).
24. Esch, T. et al. World settlement footprint 3D—a first three-dimensional survey of the global building stock. *Remote Sens. Environ.* **270**, 112877 (2022).
25. Tang, W., Yang, K., Qin, J., Li, X. & Niu, X. A 16-year dataset (2000–2015) of high-resolution (3 h, 10 km) global surface solar radiation. *Earth Syst. Sci. Data* **11**, 1905–1915 (2019).
26. Forstinger, A. et al. *Worldwide Benchmark of Modeled Solar Radiation Data IEA PVPS Task 16 Report T16-05:2023* (IEA, 2023).
27. Leduc, M., Matthews, H. D. & de Elía, R. Regional estimates of the transient climate response to cumulative CO₂ emissions. *Nat. Clim. Change* **6**, 474–478 (2016).
28. Ritchie, P. D., Clarke, J. J., Cox, P. M. & Huntingford, C. Overshooting tipping point thresholds in a changing climate. *Nature* **592**, 517–523 (2021).
29. Armstrong McKay, D. I. et al. Exceeding 1.5 °C global warming could trigger multiple climate tipping points. *Science* **377**, eabn7950 (2022).
30. Li, J., Huang, X., Tu, L., Zhang, T. & Wang, L. A review of building detection from very high resolution optical remote sensing images. *GISci. Remote Sens.* **59**, 1199–1225 (2022).
31. Cultice, B., Irwin, E. & Jones, M. Accounting for spatial economic interactions at local and meso scales in integrated assessment model (IAM) frameworks: challenges and recent progress. *Environ. Res. Lett.* **18**, 035009 (2023).
32. Aryanpur, V., O’Gallachoir, B., Dai, H., Chen, W. & Glynn, J. A review of spatial resolution and regionalisation in national-scale energy systems optimisation models. *Energy Strat. Rev.* **37**, 100702 (2021).
33. Kapsalis, V. et al. Critical assessment of large-scale rooftop photovoltaics deployment in the global urban environment. *Renew. Sustain. Energy Rev.* **189**, 114005 (2024).
34. Senyagwa, J. *Africa Energy Outlook 2022* (IEA, 2022).
35. Molnár, G., Ürge-Vorsatz, D. & Chatterjee, S. Estimating the global technical potential of building-integrated solar energy production using a high-resolution geospatial model. *J. Clean. Prod.* **375**, 134133 (2022).
36. Walch, A., Castello, R., Mohajeri, N. & Scartezzini, J.-L. Big data mining for the estimation of hourly rooftop photovoltaic potential and its uncertainty. *Appl. Energy* **262**, 114404 (2020).
37. Project Sunroof (Google, accessed 15 August 2024); <https://sunroof.withgoogle.com/>
38. Hasanuzzaman, M., Malek, A., Islam, M., Pandey, A. & Rahim, N. Global advancement of cooling technologies for PV systems: a review. *Sol. Energy* **137**, 25–45 (2016).
39. Peters, I. M. & Buonassisi, T. Energy yield limits for single-junction solar cells. *Joule* **2**, 1160–1170 (2018).
40. Peters, I. M. & Buonassisi, T. The impact of global warming on silicon PV energy yield in 2100. In *Proc. IEEE 46th Photovoltaic Specialists Conference (PVSC)* 3179–3181 (IEEE, 2019).
41. Jacobson, M. Z. & Jadhav, V. World estimates of PV optimal tilt angles and ratios of sunlight incident upon tilted and tracked PV panels relative to horizontal panels. *Sol. Energy* **169**, 55–66 (2018).
42. Creutzig, F. et al. The underestimated potential of solar energy to mitigate climate change. *Nat. Energy* **2**, 17140 (2017).
43. Liu, L. et al. Potential contributions of wind and solar power to China’s carbon neutrality. *Resour. Conserv. Recycl.* **180**, 106155 (2022).
44. Wolske, K. S., Gillingham, K. T. & Schultz, P. W. Peer influence on household energy behaviours. *Nat. Energy* **5**, 202–212 (2020).
45. Barton-Henry, K., Wenz, L. & Levermann, A. Decay radius of climate decision for solar panels in the city of Fresno, USA. *Sci. Rep.* **11**, 8571 (2021).
46. Sunter, D. A., Castellanos, S. & Kammen, D. M. Disparities in rooftop photovoltaics deployment in the United States by race and ethnicity. *Nat. Sustain.* **2**, 71–76 (2019).

Publisher's note Springer Nature remains neutral with regard to jurisdictional claims in published maps and institutional affiliations.

Open Access This article is licensed under a Creative Commons Attribution-NonCommercial-NoDerivatives 4.0 International License, which permits any non-commercial use, sharing, distribution and reproduction in any medium or format, as long as you give appropriate credit to the original author(s) and the source, provide a link to the Creative Commons licence, and indicate if you modified the licensed material. You do not have permission under this licence to share adapted material derived from this article or parts of it. The images or other third party material in this article are included in the article's Creative Commons licence, unless indicated otherwise in a credit line to the material. If material is not included in the article's Creative Commons licence and your intended use is not permitted by statutory regulation or exceeds the permitted use, you will need to obtain permission directly from the copyright holder. To view a copy of this licence, visit <http://creativecommons.org/licenses/by-nc-nd/4.0/>.

¹Key Laboratory of Virtual Geographic Environment (Ministry of Education of PRC), Nanjing Normal University, Nanjing, China. ²Potsdam Institute for Climate Impact Research, Potsdam, Germany. ³Sustainability Economics of Human Settlements, Technical University Berlin, Berlin, Germany. ⁴Earth System Modelling, School of Engineering and Design, Technical University of Munich, Munich, Germany. ⁵Jiangsu Center for Collaborative Innovation in Geographical Information Resource Development and Application, Nanjing, China. ⁶International Research Center of Big Data for Sustainable Development Goals, Beijing, China. ⁷Institute of High Performance Computing (IHPC), Agency for Science, Technology and Research (A*STAR), Singapore, Republic of Singapore. ⁸Institute of Remote Sensing and Geographical Information System, School of Earth and Space Sciences, Peking University, Beijing, China. ⁹Bennett Institute for Innovation and Policy Acceleration, University of Sussex Business School, Brighton, UK. ¹⁰National Tibetan Plateau Data Center (TPDC), State Key Laboratory of Tibetan Plateau Earth System, Environment and Resources (TPESER), Institute of Tibetan Plateau Research, Chinese Academy of Sciences, Beijing, China. ¹¹Department of Geography, The University of Hong Kong, Hong Kong, China. ¹²Institute for Climate and Carbon Neutrality, The University of Hong Kong, Hong Kong, China. ¹³Department of Civil and Environmental Engineering, The Hong Kong University of Science and Technology, Hong Kong, China. ¹⁴State Key Laboratory of Numerical Modeling for Atmospheric Sciences and Geophysical Fluid Dynamics (LASG), Institute of Atmospheric Physics, Chinese Academy of Sciences, Beijing, China. ¹⁵Department of Earth System Science, Institute for Global Change Studies, Ministry of Education Ecological Field Station for East Asian Migratory Birds, Tsinghua University, Beijing, China. ¹⁶School of Geography and Ocean Science, Nanjing University, Nanjing, China. ¹⁷Jiangsu Provincial Key Laboratory of Geographic Information Science and Technology, Nanjing, China. ¹⁸School of Civil Engineering and Surveying and Mapping Engineering, Jiangxi University of Science and Technology, Ganzhou, China. ¹⁹School of Resources and Geosciences, China University of Mining and Technology, Xuzhou, China. ²⁰College of Geography and Remote Sensing, Hohai University, Nanjing, China. ²¹Geographic Science College, Nanjing University of Information Science and Technology, Nanjing, China. ²²Research Center for Environment and Health, Zhongnan University of Economics and Law, Wuhan, China. ²³School of Business Administration, Zhongnan University of Economics and Law, Wuhan, China. ²⁴School of Transportation and Geomatics Engineering, Shenyang Jianzhu University, Shenyang, China. ²⁵Senseable City Laboratory, Department of Urban Studies and Planning, Massachusetts Institute of Technology, Cambridge, MA, USA. ²⁶Istituto di Informatica e Telematica del CNR, Pisa, Italy. ²⁷Research Institute of Carbon Neutralization Development, School of Mathematical Sciences, Jiangsu University, Zhenjiang, China. ²⁸Key Laboratory for NSLSCS, Ministry of Education, School of Mathematical Sciences, Nanjing Normal University, Nanjing, China. ²⁹Department of Building Environment and Energy Engineering, The Hong Kong Polytechnic University, Kowloon, Hong Kong, China. ³⁰Future Energy Center, Mälardalen University, Västerås, Sweden. ³¹These authors contributed equally: Zhixin Zhang, Zhen Qian.

✉e-mail: chenmin0902@njnu.edu.cn

Methods

Two-stage process for global rooftop area estimation

The global rooftop area estimation followed a two-stage process (Extended Data Fig. 1): (1) a top-down approach using deep learning to quantify the rooftop area in selected representative regions from high-resolution remote sensing imagery and (2) a bottom-up approach using random forest ensembles and various geospatial datasets to extrapolate rooftop area estimates at a global scale.

In the top-down stage, we used the SegFormer model, a state-of-the-art Vision Transformer-based deep learning model in computer vision⁴⁷. The choice of this architecture was motivated by its capacity to process large datasets and its ability to capture global context while handling complex patterns and long-range dependencies—crucial for large-scale building identification⁴⁸. For pretraining, we used publicly available benchmark datasets focused on building identification^{13,49} (Supplementary Table 1). These datasets, generated by various institutions between 2013 and 2020, cover ~2,500 km² across diverse regions with varying spatial resolutions, ranging from very fine (0.1 m per pixel) to coarser (3 m per pixel). The selected datasets represent a wide range of global regions and building types, including urban, suburban and rural areas, as well as a mix of built-up and natural landscapes. They also cover various urban layouts and densities, offering high-resolution imagery that captures different architectural styles and building sizes. This broad representation ensures that the model is trained across diverse environments, enhancing its ability to generalize to different geographic contexts.

For fine-tuning the deep learning model, we used high-resolution Google Earth imagery with a consistent spatial resolution of 1.2 m. Google Earth imagery is obtained through the Google Static Map API, which applies rigorous sifting and preprocessing to produce cloud-free, high-quality images⁵⁰. The imagery is sourced from a combination of airborne and satellite platforms, including WorldView, QuickBird, IKONOS, GeoEye-1, Pleiades, SuperView-1 and Kompsat-3A, resulting in harmonized imagery⁵¹. Further details on the SegFormer architecture, along with the pretraining and fine-tuning processes, are provided in Supplementary Note 3.

We applied the trained deep learning model to quantify rooftop area in 1,724 cities, where ‘city’ refers to administrative divisions sourced from the database of global administrative areas (Extended Data Fig. 4). These regions were strategically selected using a spatial sampling scheme, with cities treated as sample units. The objective was to maximize the distance between samples to ensure representativeness, optimized using a simulated annealing algorithm⁵². To further enhance the geographic and environmental diversity of the selected regions, we first stratified the global grids using *K*-means clustering, based on natural and human characteristics of each grid (Supplementary Fig. 6 and Supplementary Table 2). The optimal number of clusters for the *K*-means algorithm was determined using silhouette coefficients. After stratification, spatial sampling was performed within each stratum.

In the bottom-up stage, we collected multi-source geospatial datasets and aggregated them as statistical variables—such as built-up proportion, night-time light intensity, road length, population, tree-cover proportion, terrain elevation, terrain slope and geographical coordinates (Supplementary Fig. 2 and Supplementary Table 2)—into global discrete spatial grids. These variables are strong predictors of rooftop areas because they capture both human activity and the physical characteristics of the environment^{9,10}. For instance, night-time light intensity is often correlated with urbanization and building density, while terrain elevation and slope can influence building placement and rooftop orientation. Each spatial grid covered an area of 1 km² and was based on the world Mollweide equal area projection (EPSG: 6933). To model the nonlinear relationship between the rooftop area and these geospatial variables, we aggregated the rooftop area determined in the selected regions into the corresponding grids. Grids lacking

high-resolution remote sensing imagery were excluded, resulting in 8.5 million grid samples. The rooftop area was treated as the dependent variable in these samples, while the other statistical variables were used as independent variables.

Considering the spatial heterogeneity of grid cell variables and addressing the long-tail regression modelling issue, we developed both regression- and classification-oriented random forest models at both continental and global scales. The trained random forest ensembles were then applied to estimate the global rooftop area using a set of global independent variables. Further details on the random forest ensemble can be found in Supplementary Note 4. In the postprocessing stage, a water map was used to refine the initial estimates by assigning a rooftop area of 0 m² to grids that were 100% water-covered based on land use and land cover data.

Evaluation of estimated global rooftop area

The evaluation involved assessing the accuracy of the deep learning model in the top-down stage and the random forest ensemble in the bottom-up stage using independent test datasets. Additionally, the quality of the global rooftop area estimates was evaluated through qualitative and quantitative comparisons with reference datasets.

To evaluate the performance of the deep learning model, we created 386 plots, each covering an area of 1 km² (Extended Data Fig. 2b). These plots were selected to ensure global representation, with two plots randomly distributed within the built-up areas of each country. High-resolution remote sensing images were obtained for all 386 plots and each was manually labelled to identify rooftop areas. The average rooftop area across the plots was 0.14 ± 0.10 km² (mean \pm s.d.), with a maximum of 0.53 km². These plots span different countries and geographic regions, encompassing a wide range of building distributions and densities, providing a comprehensive evaluation. The plots were further divided into 2,951 image patches, each processed to match the size and colour bands of the training images used for the deep learning model, ensuring consistency in the validation process (examples in Supplementary Fig. 1). This test dataset was kept independent from the training data to prevent bias in the performance assessment of the model.

Against the labelled image patches, the deep learning model successfully identified 76% of the rooftops (true-positive rate), with a 2.7% false-positive rate where non-rooftop objects were mistakenly identified as rooftops. This level of performance is acceptable for building identification at a global scale: we compared the MBF and GBF—currently state-of-the-art building footprint datasets—against our test dataset. MBF had a true-positive identification rate of 61.6% and a false-positive rate of 4%, while GBF had a true-positive rate of 66.5% and a false-positive rate of 3.8%.

Additionally, we compared the rooftop area quantified by the deep learning model with the manually labelled rooftop area for each image patch. Overall, the predictions of the model showed a strong correlation with the actual data, with an r^2 value of 0.93 and a slope of 1.04 across all test samples (Extended Data Fig. 3a). However, we observed variations in prediction accuracy across different macroregions (Extended Data Fig. 3b–u): the model performed with greater accuracy in economically developed regions, where r^2 values exceeded 0.95. In contrast, accuracy decreased in less economically developed regions, with r^2 values around 0.9. These discrepancies could be due to the varying ability of the model to recognize landscapes that differ notably across regions.

To evaluate the accuracy of the global rooftop area estimation by the random forest ensemble, we randomly selected 16,000 grids across various macroregions (800 grid samples per macroregion). These grids were not part of the training process of the random forest model. We used deep learning and high-resolution remote sensing imagery to quantify the rooftop area within these grids. The rooftop area determined from the images was then compared with the

estimates generated by the random forest ensemble. Our results demonstrated a high level of accuracy, with an r^2 value of 0.89 and a slope of 0.87 (Extended Data Fig. 5), indicating strong consistency between the estimated and observed rooftop area, although with a slight underestimation.

However, the results also indicated a drop in accuracy for the Pacific Islands ($r^2 = 0.61$, bias error = 55%; Extended Data Fig. 5c) and Western Asia ($r^2 = 0.67$, bias error = 24%; Extended Data Fig. 5k). This suggests potential limitations in capturing relevant factors in these regions, probably due to a lack of local data in the training set, especially in areas where high-resolution remote sensing imagery is scarce. The bias error here is defined as the relative bias, normalized by the absolute value of the sum of the observed rooftop areas and is calculated using the following equation⁵³:

$$\text{bias} = \frac{|\sum_N (Y_{\text{obs}} - Y_{\text{pred}})|}{|\sum_N Y_{\text{obs}}|} \quad (1)$$

We also compared the estimated and observed rooftop area by identifying deviations (residuals) across the 16,000 test grids. The results revealed a correlation between rooftop area and residuals: grids with larger rooftop area tended to exhibit greater residuals. Specifically, for grids with rooftop area ranging from 0.01 to 1 km², the variation in residuals was substantial, showing a slight underestimation (Extended Data Fig. 6a). Residuals demonstrated a bell-shaped normal distribution, with most clustering between ±5,000 m² (Extended Data Fig. 6b). Further examination of the global distribution of estimated rooftop area revealed that most 1-km² grids had rooftop area <0.4 km² (Extended Data Fig. 7a). This consistent pattern of rooftop area distribution was evident across various scales (Extended Data Fig. 7b–u).

To assess the quality of our global rooftop area estimates, we compared them with several reference datasets, including GBF, MBF, GHSL and WSF3D. The qualitative characteristics of these reference datasets are described in Supplementary Table 10. While GBF and MBF represent advanced building footprint products, their coverage is incomplete, omitting extensive areas across multiple continents (Supplementary Fig. 7). For example, aggregated GBF lacks large portions of North America, Europe, East Asia and Australia, while MBF lacks coverage over China, Russia and parts of Europe. Compared with these datasets, our estimates provide globally seamless coverage, produced through the two-stage method. By incorporating natural and human-related datasets from 2020, our estimates capture current urban development and building areas, with the exception of the digital elevation model from SRTM v.4 (collected in the 2000s), which remains appropriate given the relatively stable nature of global terrain over time.

For the quantitative comparison, we conducted a detailed grid-level and continental-level analysis. Owing to the limited coverage and potential spatial completeness issues in the GBF and MBF datasets, we restricted our comparison to grids that contain building areas in both datasets. For comparisons with GHSL and WSF3D, we used global grids. The results of these grid comparisons are shown in Extended Data Fig. 8, where our global rooftop area estimates exhibit high correlations with the reference datasets. However, our estimates tend to be lower than those of the reference datasets, as reflected by the slopes of the linear fits, all of which are <1 (0.71 for GBF, 0.83 for MBF, 0.58 for GHSL and 0.72 for WSF3D). This underestimation trend is consistent with our test dataset results, which also produced a slope of 0.87. Among the reference datasets, the comparison with GHSL shows the largest discrepancies, with an r^2 value of 0.76 and a bias error of 37%. We attribute this to the tendency of GHSL to overestimate rooftop areas by including impervious surfaces.

We also evaluated the estimates across different macroregions. The grid-level analysis shows high correlations with both GHSL and WSF3D (Supplementary Figs. 8 and 9). However, in less economically developed regions—such as the Pacific Islands, Central Asia and various

regions of Africa (Eastern, Southern, Western and Middle Africa)—we observed relatively lower r^2 values and higher biases. Furthermore, the comparison of total rooftop area across macroregions, summarized in Supplementary Table 11, shows that WSF3D and our estimates are generally consistent, while the total area of GHSL is substantially higher. This trend persists in less economically developed regions, where our estimates are typically lower. The potential underestimation could be due to geographic variations in building identification accuracy, as previously discussed. At the global level, our estimates closely align with those of WSF3D, although the totals of WSF3D are slightly higher. In contrast, the global area of GHSL is substantially larger, probably indicating overestimation. Compared with a previous study that estimated a total global rooftop area of 193,875 km² (which was noted for systematic underestimation)⁹, our estimates (286,393 km²) demonstrate improved alignment with reference datasets. Although slight underestimation remains in our results, we have mitigated many of the issues identified in earlier studies.

Assessment of electricity generation and carbon mitigation potential

Unified assumptions were applied to the RPV systems in this study. On the basis of the current technical level of the PV industry⁵⁴, the scale and performance parameters of PV applications were determined (Supplementary Tables 12 and 13), including a PV panel conversion efficiency of 20%, an overall PV system efficiency of 0.8 and a rated power of 200 W m⁻². All the PV panels in the system were assumed to be fixed horizontally. The available installed capacity of RPVs, essential to determine their potential for electricity generation and carbon mitigation, was calculated by converting the total rooftop area into the available rooftop area using a scaling factor. The factor typically considers a range of geographical constraints for RPV system installation, such as the societal function, rooftop slope, orientation, shadows and obstacles of the building. On the basis of a literature review (Supplementary Table 3), the scaling factor used in the main results was assumed to be 30%.

The potential installed capacity, $P_{\text{installed}}$, was calculated using equation (2) as follows:

$$P_{\text{installed}} = P_{\text{rated}} \times S_{\text{rooftop}} \times C_{\text{scaling}} \quad (2)$$

where P_{rated} is the rated power of the PV panel, S_{rooftop} is the total rooftop area obtained from the global rooftop area estimation and C_{scaling} is the scaling factor for calculating the available rooftop area for RPV installation.

The potential electricity generation P_{power} of the RPVs was estimated using equation (3):

$$P_{\text{power}} = S_{\text{rooftop}} \times C_{\text{scaling}} \times \text{GHI} \times C_{\text{PV}} \times K \quad (3)$$

where GHI is the global horizontal irradiance received by the surface. We took the average values from 2010 to 2018 to represent the general radiation conditions at different assessment times. C_{PV} is the conversion efficiency of the PV panel and K is the overall efficiency of the RPV system.

In this study, our focus was on the electricity generation stage of RPV systems, excluding consideration of other life-cycle stages. This decision stems from the considerably lower life-cycle carbon emissions of RPV systems compared with the emissions mitigated during the operational stage⁵⁵ (Supplementary Table 14). We followed the baseline methodology⁵⁶ proposed by the United Nations Framework Convention on Climate Change (UNFCCC) to measure the environmental benefits of renewable energy projects. The baseline methodology provides a simplified analytical framework and facilitates a uniform comparison across different projects, thereby promoting the development of related policies. The carbon emissions mitigated by RPV power

replacing grid power were calculated using the baseline emission factors of the national grid^{57,58}. The baseline emission factors included the operating margin (OM) and build margin (BM). While OM represents the cohort of existing power plants most affected (reduced) by the project (generally high-emission or high-cost power plants), BM represents the cohort of prospective/future power plants whose construction and operation could be affected by renewable energy projects, based on an assessment of planned and expected new generation capacity. The combined margin (CM), obtained from the weighted average of the OM and BM, represents the overall impact of both aspects, and reflects the existing carbon intensity of the national grid. Because the electricity generated through RPVs is considered clean energy, the CM factor, $EF_{grid,CM}$, can be used as the carbon mitigation factor, $EF_{PV,mitigation}$, of the RPV system. The calculations were conducted using equation (4) as follows:

$$EF_{PV,mitigation} = EF_{grid,CM} = EF_{grid,OM} \times W_{OM} + EF_{grid,BM} \times W_{BM} \quad (4)$$

where $EF_{grid,OM}$ is the OM factor and $EF_{grid,BM}$ is the BM factor. W_{OM} is the weight of the OM factor and W_{BM} is the weight of the BM factor. The values for PV projects were set to 0.75 and 0.25, respectively, based on the UNFCCC methodologies⁵⁸.

According to the carbon mitigation factors of the RPV system for different power grids, carbon mitigation, $P_{carbon,mitigation}$, was calculated according to equation (5):

$$P_{carbon,mitigation} = P_{power} \times EF_{PV,mitigation} \quad (5)$$

The selected baseline emission factors reflect the average conditions of national grids in recent years and are updated at least every 2 years (ref. 58). For assessment purposes, we designated 2020 as the base year. Future baseline emission factors are subject to alterations in the power structure of each country. We assume that this change is consistent with the trend in grid carbon intensity projected by the International Energy Agency for 2020–2050⁵⁹. On the basis of this assumption, we obtained future changes in the $EF_{PV,mitigate}$ under three climate policy scenarios: STEPS, SDS and NZE (Supplementary Notes 1 and 2 and Supplementary Fig. 4).

In this study, the energy assessment relied on conversion factors, such as rooftop area availability and PV panel efficiency, using harmonized global reference values. We acknowledge the importance of examining these factors at the regional level. However, such a detailed analysis was beyond the scope of this study. Sensitivity analyses were included to mitigate this limitation and provide an initial understanding of how variations in these factors could affect our main results (Supplementary Tables 4–6).

Assessment of global and regional warming mitigation potential
The relationship between global warming and cumulative carbon emissions was established using the well-documented TCRE metric. TCRe is estimated as the change in global surface air temperature per cumulative CO₂ emissions⁶⁰. It considers both physical climate processes and the dynamics of land and ocean carbon sinks, presumed to be constant over time and independent of emission pathways⁶¹. The relationship between regional climate warming and carbon emissions was established using the RTCRE, which describe changes on a regional scale. In this study, the TCRE was scaled to a regional scale to generate an RTCRE using simple pattern scaling⁶². According to a previous study²⁷, RTCRE can be calculated using equation (6):

$$RTCRE(m, x, t) = \frac{\Delta T(m, x, t)}{E(m, t)} \quad (6)$$

where $\Delta T(m, x, t)$ is the temperature change simulated by the m th model in the ensemble, for the spatial domain x at time t . Parameter $E(m, t)$ is

the diagnostic value of the cumulative CO₂ emissions (calculated as the sum of the annual changes in atmospheric CO₂ concentration and the CO₂ uptake by ocean and land carbon sinks) of the model.

We used the 1pctCO₂ simulations from nine ESMs with dynamic carbon cycle from the CMIP6 archive. The ensemble comprised ACCESS-ESM1.5, BCC-CSM2-MR, CanESM5, CESM2, IPSL-CM6A-LR, MIROC-ES2L, MPI-ESM1.2-LR, NorESM2-LM and UKESM1-0-LL. We followed the standard method⁶³ for calculating $\Delta T(m, x, t)$, averaging over a 20-yr window (years 60–79) centred on the year of the CO₂ doubling (year 70). We applied this calculation to the spatial temperature fields from each model and then calculated the ensemble mean of the nine models. We considered the ensemble mean as the best estimate of the RTCRE values and represented the uncertainty range using one standard deviation of the model responses.

After obtaining the RTCRE, the warming mitigation potential, $P_{warming,mitigate}$ of RPVs were calculated according to equation (7):

$$P_{warming,mitigate} = P_{carbon,mitigate} \times RTCRE \quad (7)$$

While the concept of TCRe simplifies the relationship between CO₂ emissions and global warming into a linear model, this relationship is fraught with uncertainties owing to numerous complex factors, such as the effects of permafrost melting and non-CO₂ GHGs⁶⁴. Land surface changes caused by PV panels could also impact the regional climate to some extent by redistributing surface energy, water fluxes and even atmospheric circulation⁶⁵; however, global climate change mitigation should be dominated by carbon emission reductions. In addition, future solar energy generation could be modulated by climate change to some extent⁶⁶. Future climate change impacts should be considered for finer assessments.

Reporting summary

Further information on research design is available in the Nature Portfolio Reporting Summary linked to this article.

Data availability

The estimation results⁶⁷ of global rooftop area in our study are available via National Tibetan Plateau and Third Pole Environment Data Center at <https://doi.org/10.11888/HumanNat.tpdC.302010>. Source data are provided in Methods and Supplementary Information.

Code availability

The code used to manipulate the data and generate the results is available via Zenodo at <https://doi.org/10.5281/zenodo.14749963> (ref. 68).

References

47. Xie, E. et al. SegFormer: simple and efficient design for semantic segmentation with transformers. *Adv. Neural Info. Proc. Syst.* **34**, 12077–12090 (2021).
48. Wang, L., Fang, S., Meng, X. & Li, R. Building extraction with vision transformer. *IEEE Trans. Geosci. Remote Sens.* **60**, 5625711 (2022).
49. Ji, S., Wei, S. & Lu, M. Fully convolutional networks for multisource building extraction from an open aerial and satellite imagery data set. *IEEE Trans. Geosci. Remote Sens.* **57**, 574–586 (2018).
50. Pulighe, G., Baiocchi, V. & Lupia, F. Horizontal accuracy assessment of very high resolution Google Earth images in the city of Rome, Italy. *Int. J. Digit. Earth* **9**, 342–362 (2016).
51. Li, Z. et al. SinoLC-1: the first 1-meter resolution national-scale land-cover map of China created with the deep learning framework and open-access data. *Earth Syst. Sci. Data Discuss.* **15**, 4749–4780 (2023).
52. Qian, Z. et al. Simultaneous extraction of spatial and attributional building information across large-scale urban landscapes from high-resolution satellite imagery. *Sustain. Cities Soc.* **106**, 105393 (2024).

53. Mugabowindekwe, M. et al. Nation-wide mapping of tree-level aboveground carbon stocks in Rwanda. *Nat. Clim. Change* **13**, 91–97 (2023).
54. Khalid, A. M., Mitra, I., Warmuth, W. & Schacht, V. Performance ratio—crucial parameter for grid connected PV plants. *Renew. Sustain. Energy Rev.* **65**, 1139–1158 (2016).
55. Wang, M., Mao, X., Gao, Y. & He, F. Potential of carbon emission reduction and financial feasibility of urban rooftop photovoltaic power generation in Beijing. *J. Clean. Prod.* **203**, 1119–1131 (2018).
56. *Methodologies, Standardized Baselines and Methodological Tools* (UNFCCC, 2024); <https://unfccc.int/process-and-meetings/the-paris-agreement/paris-agreement-crediting-mechanism/methodologies>
57. IFI TWG. *Harmonized IFI Default Grid Factors 2021 v3.1* (UNFCCC, 2021); <https://unfccc.int/documents/461676>
58. IFI TWG. *Methodological Approach for the Common Default Grid Emission Factor Dataset* (UNFCCC, 2022); <https://unfccc.int/documents/228111>
59. *Global Average Carbon Intensity of Electricity Generation in the Stated Policies, Sustainable Development and Net Zero Scenarios* (IEA, 2021).
60. IPCC. *Climate Change 2013: The Physical Science Basis* (eds Stocker, T. F. et al.) (Cambridge Univ. Press, 2013).
61. Millar, R. J. et al. Emission budgets and pathways consistent with limiting warming to 1.5 °C. *Nat. Geosci.* **10**, 741–747 (2017).
62. Tebaldi, C. & Arblaster, J. M. Pattern scaling: its strengths and limitations, and an update on the latest model simulations. *Clim. Change* **122**, 459–471 (2014).
63. Arora, V. K. et al. Carbon-concentration and carbon-climate feedbacks in CMIP6 models and their comparison to CMIP5 models. *Biogeosciences* **17**, 4173–4222 (2020).
64. Rogelj, J., Forster, P. M., Kriegler, E., Smith, C. J. & Séférian, R. Estimating and tracking the remaining carbon budget for stringent climate targets. *Nature* **571**, 335–342 (2019).
65. Hu, A. et al. Impact of solar panels on global climate. *Nat. Clim. Change* **6**, 290–294 (2016).
66. Liu, L. et al. Climate change impacts on planned supply–demand match in global wind and solar energy systems. *Nat. Energy* **8**, 870–880 (2023).
67. *Global Rooftop Area Dataset* (2020) (National Tibetan Plateau/Third Pole Environment Data Center, 2025); <https://cstr.cn/18406.11.HumanNat.tpdc.302010>
68. Qian, Z. Core scripts for “Worldwide rooftop photovoltaic electricity generation may mitigate global warming”. Zenodo <https://doi.org/10.5281/zenodo.14749963> (2025).

Acknowledgements

This work is supported by the National Natural Science Foundation of China for Distinguished Young Scholars (42325107, awarded to M.C.), the National Natural Science Foundation of China (W2412152, awarded to M.C.) and the International Research Center of Big Data for Sustainable Development Goals (CBAS2022GSP08, awarded to M.C.).

Author contributions

M.C. proposed the research idea and conceptual framework. Z.Z., Z.Q. and M.C. designed the research. Z.Z. and Z.Q. performed the research and wrote the first version of the paper. R.Z., F.Z., T.Z., J.L. and L.N. provided theoretical and technical guidance. W.X., F.C., W.T., L.L., J. Yang, Ye Pu, W.C., Yingxia Pu, D.L., H.Y., H.S., M.L., F.L., X.C., Z.X., T.S., K.Z., P.S., L.T., G.L. and J. Yan contributed to data production and provided feedback on the paper. All authors reviewed and approved the final paper.

Competing interests

The authors declare no competing interests.

Additional information

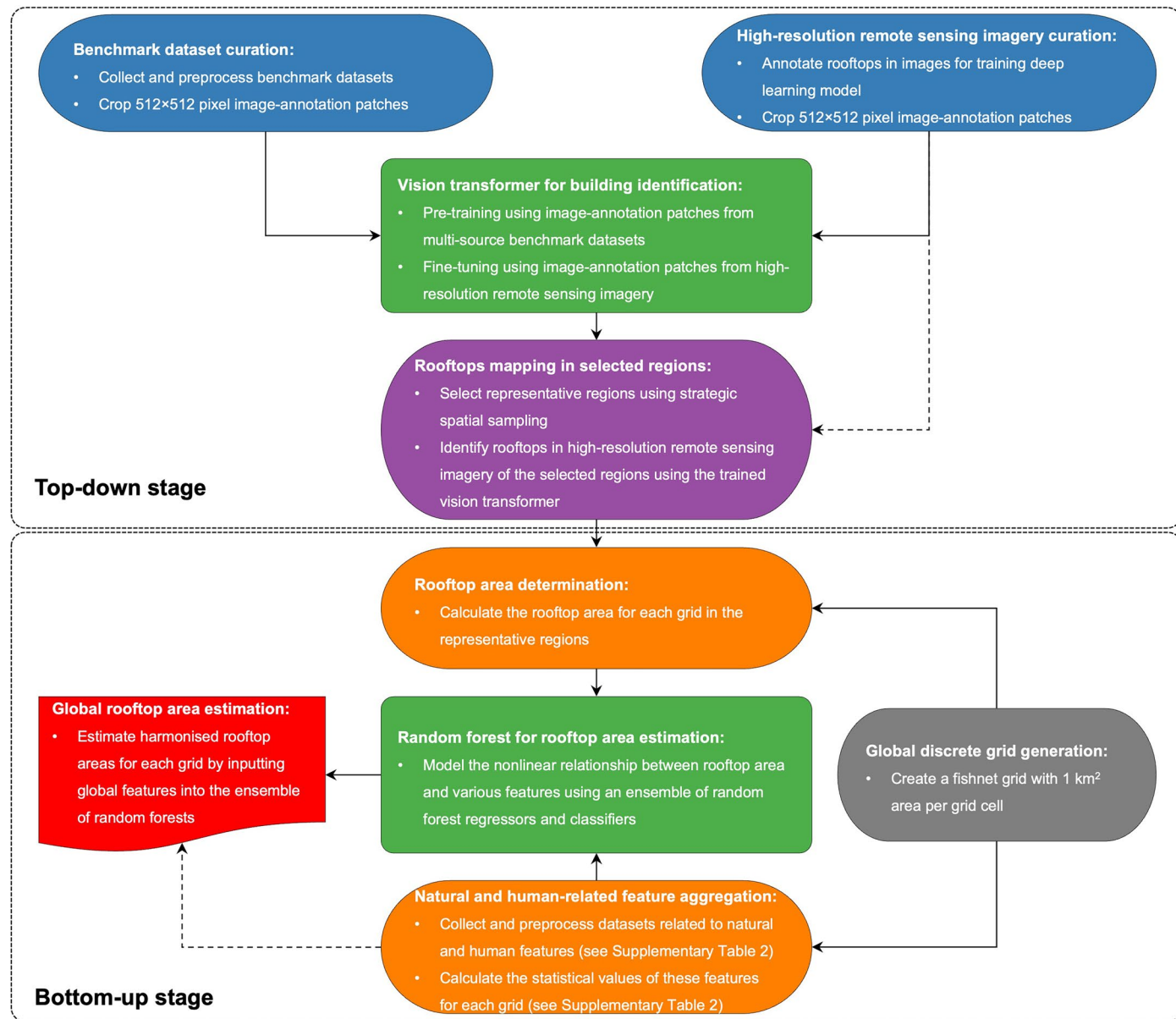
Extended data is available for this paper at <https://doi.org/10.1038/s41558-025-02276-3>.

Supplementary information The online version contains supplementary material available at <https://doi.org/10.1038/s41558-025-02276-3>.

Correspondence and requests for materials should be addressed to Min Chen.

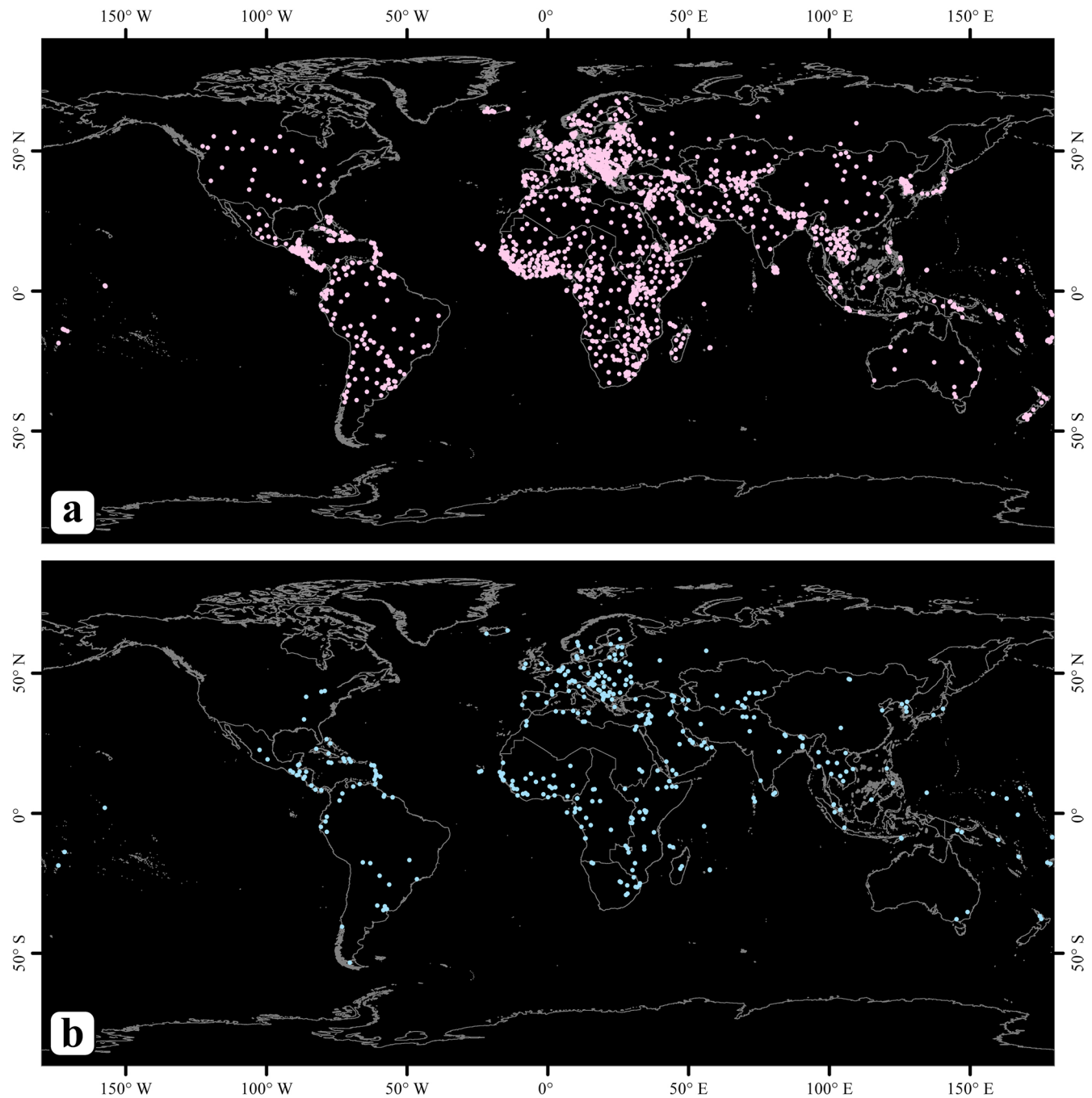
Peer review information *Nature Climate Change* thanks Pei Huang, Marion Schroedter-Homscheidt and the other, anonymous, reviewer(s) for their contribution to the peer review of this work.

Reprints and permissions information is available at www.nature.com/reprints.



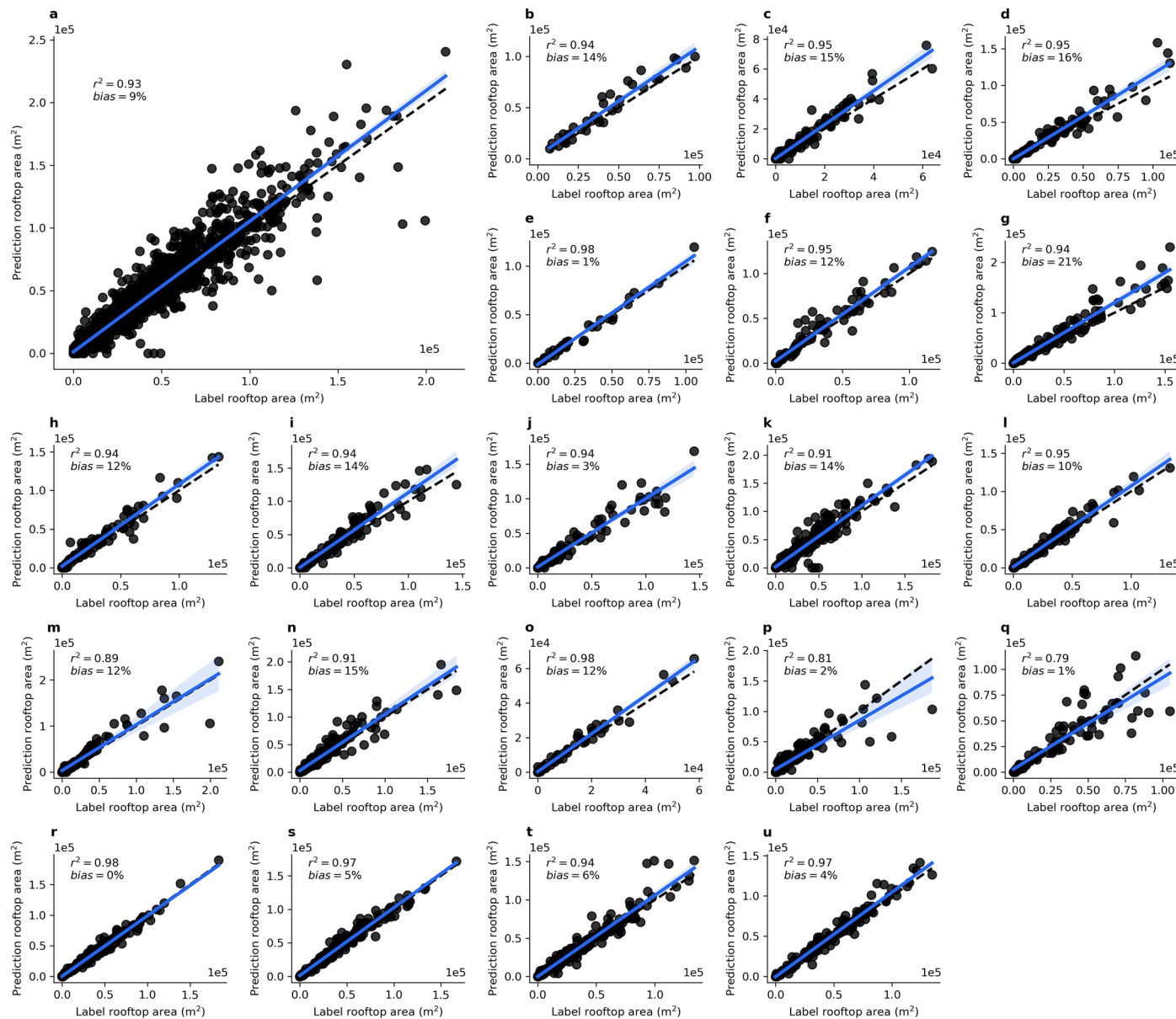
Extended Data Fig. 1 | Overview of the two-stage method for global rooftop area estimation. The top-down stage involves applying a deep learning model to high-resolution remote sensing imagery to quantify rooftop areas in selected representative regions. The bottom-up stage uses an ensemble of random forest

models to model the non-linear relationship between the rooftop areas identified in the first stage and various geospatial variables, enabling the extrapolation of rooftop area estimates at a global scale.



Extended Data Fig. 2 | Overview of training and test sites for deep learning development and evaluation. **a**, A total of 1,600 sites were randomly selected from all United Nations member countries to train the deep learning models. Half of the sites were built-up (urban) areas, and the other half were non-built-up (rural or natural) areas, with each site covering an area of 1 km². The number of sites selected from each country was based on the logarithmic scale of the land

area of each country. **b**, Spatial distribution of the test sites, covering a total of 386 km², for evaluating deep learning models. Each site had an area of 2 km² and was randomly selected from the built-up areas of each United Nations member country. This approach ensured a wide and representative sample for evaluating the accuracy of our models across various global regions.


Extended Data Fig. 3 | Evaluation of rooftop area quantification using deep learning.

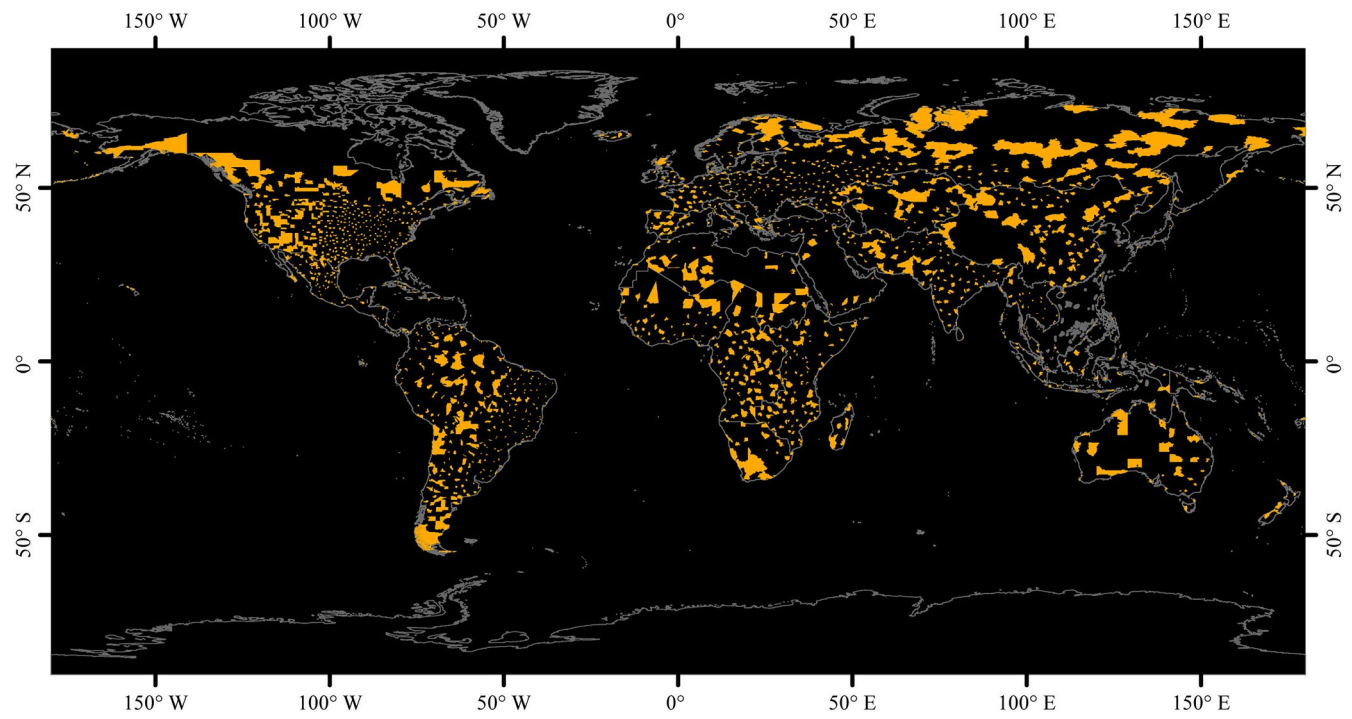
Learning. This figure evaluates the prediction accuracy of our deep learning model, which quantified rooftop area compared with manually labelled data in an independent test dataset. This comparison was conducted using randomly selected image patches, each measuring 512 × 512 pixels. **a.** Overview of all test image patches (total number = 2,951). **b-u.** Breakdown of test image patches by geographic region, showing the specific number of patches evaluated in each area. **b.** Australia and New Zealand (36 patches). **c.** Pacific Islands (136 patches).

d. Caribbean (173 patches). **e.** Northern America (36 patches). **f.** Central America (99 patches). **g.** South America (164 patches). **h.** Eastern Asia (87 patches).

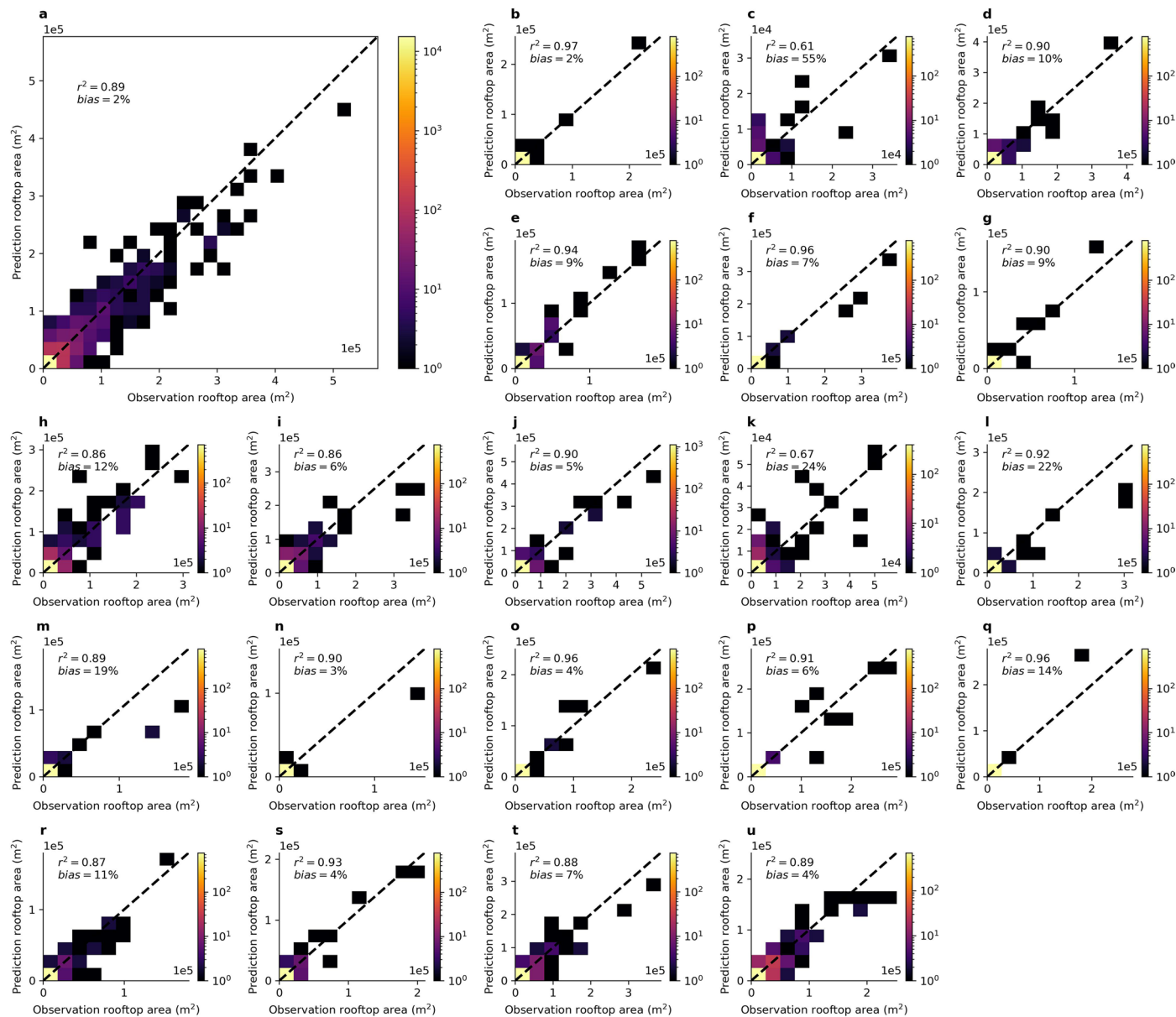
i. South-Eastern Asia (129 patches). **j.** Southern Asia (127 patches). **k.** Western Asia (266 patches). **l.** Central Asia (90 patches). **m.** Northern Africa (101 patches).

n. Eastern Africa (206 patches). **o.** Southern Africa (74 patches). **p.** Western Africa (182 patches). **q.** Middle Africa (96 patches). **r.** Northern Europe (306 patches).

s. Eastern Europe (220 patches). **t.** Southern Europe (252 patches). **u.** Western Europe (171 patches).

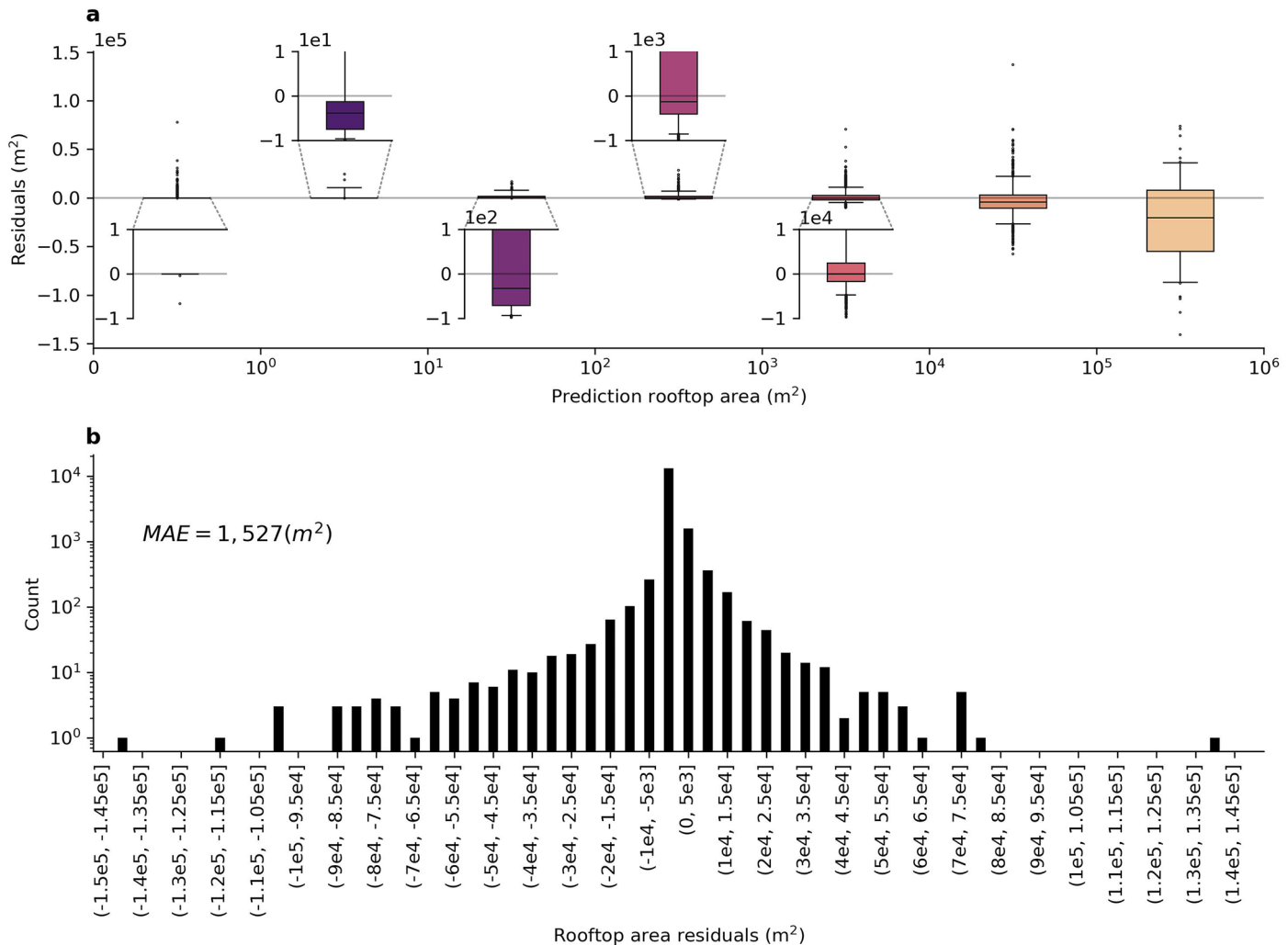


Extended Data Fig. 4 | Mapping building rooftops in selected global regions. Orange patches represent 1,724 cities across various continents and cover an extensive area of 20 million km². These regions were strategically selected for the development of predictive models aimed at estimating global rooftop area.


Extended Data Fig. 5 | Evaluation of rooftop area estimation accuracy.

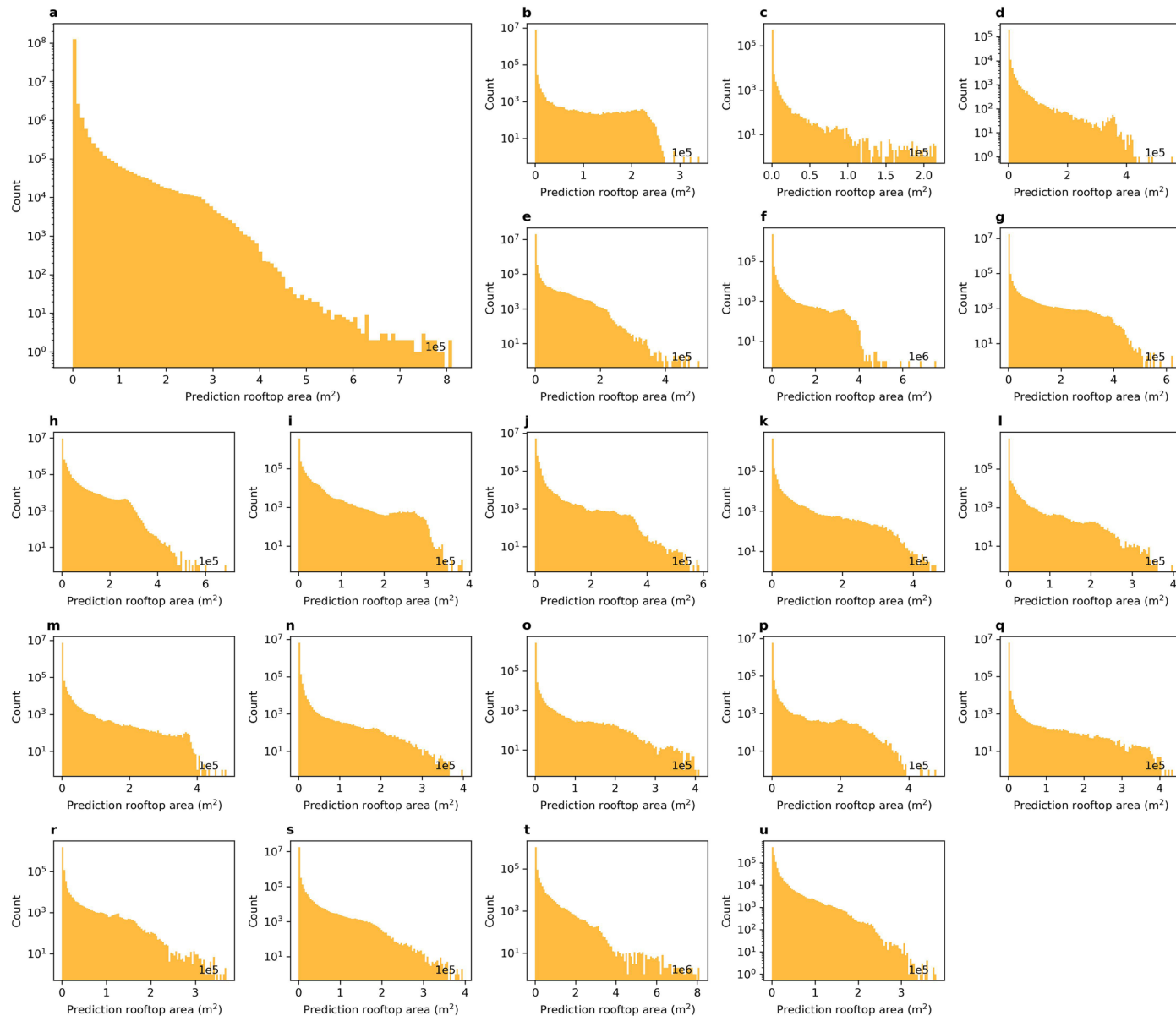
These plots present the accuracy assessments of our random forest models for estimating rooftop area compared with the actual observed rooftop area from our independent test dataset. A set of 16,000 randomly selected grid samples was used. The primary aspect of this comparison is the predictive confusion matrix, which categorizes the estimated rooftop area into 20 bins, allowing for a detailed comparison between the predictions of our model and the real rooftop

area. **a**, Overview of all test grids used in this study. **b-u**, The test grids were broken down into specific geographic regions, with each region represented by 800 grids. **b**, Australia and New Zealand. **c**, Pacific Islands. **d**, Caribbean. **e**, Northern America. **f**, Central America. **g**, South America. **h**, Eastern Asia. **i**, South-Eastern Asia. **j**, Southern Asia. **k**, Western Asia. **l**, Central Asia. **m**, Northern Africa. **n**, Eastern Africa. **o**, Southern Africa. **p**, Western Africa. **q**, Middle Africa. **r**, Northern Europe. **s**, Eastern Europe. **t**, Southern Europe. **u**, Western Europe.

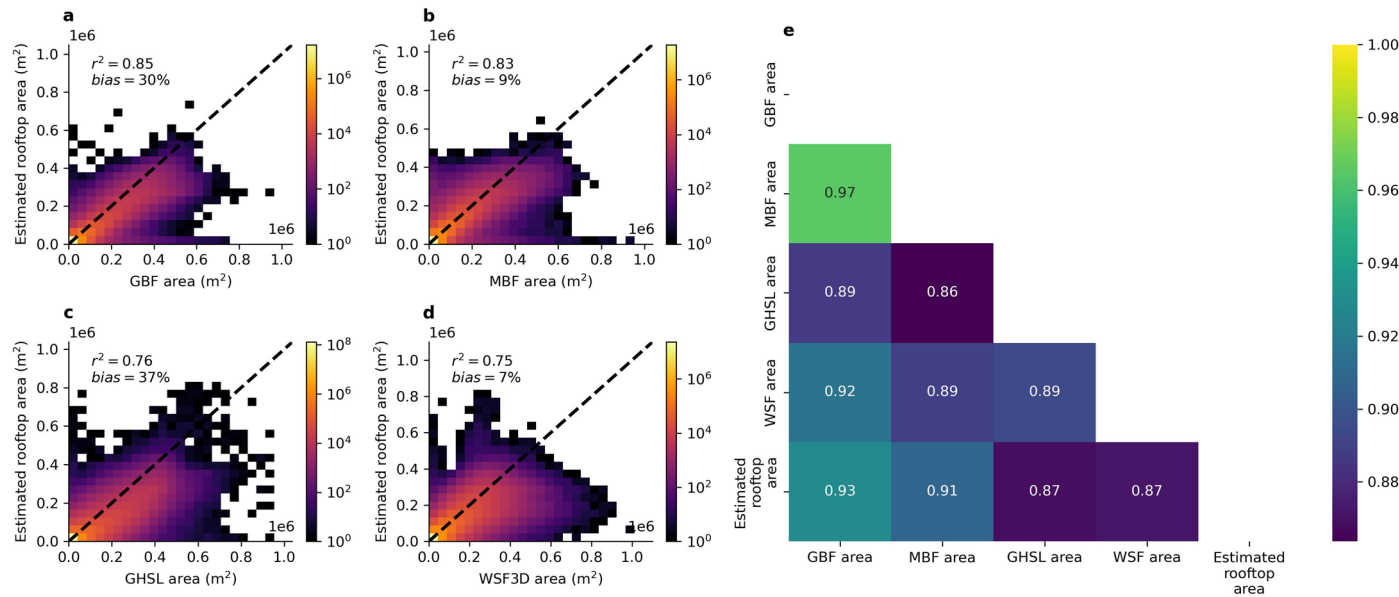

Extended Data Fig. 6 | Analysis of residuals in rooftop area estimation.

a, Residual analysis of rooftop areas at different scales using boxplots. To enhance visual clarity, the first four box plots are locally magnified. was used. In these boxplots, the lines from top to bottom represent the maximum, third quartile (upper quartile), median (middle value), first quartile (lower quartile), and

minimum value. Points scattered outside the boxplots are considered outliers, indicating values that are different from the rest. The light gray line represents a residual equal to 0. **b**, an analysis of the distribution of residuals using a histogram. This method visually represents the frequency of the residual values. Both analyses in parts a and b are based on a set of 16,000 randomly selected grid samples.

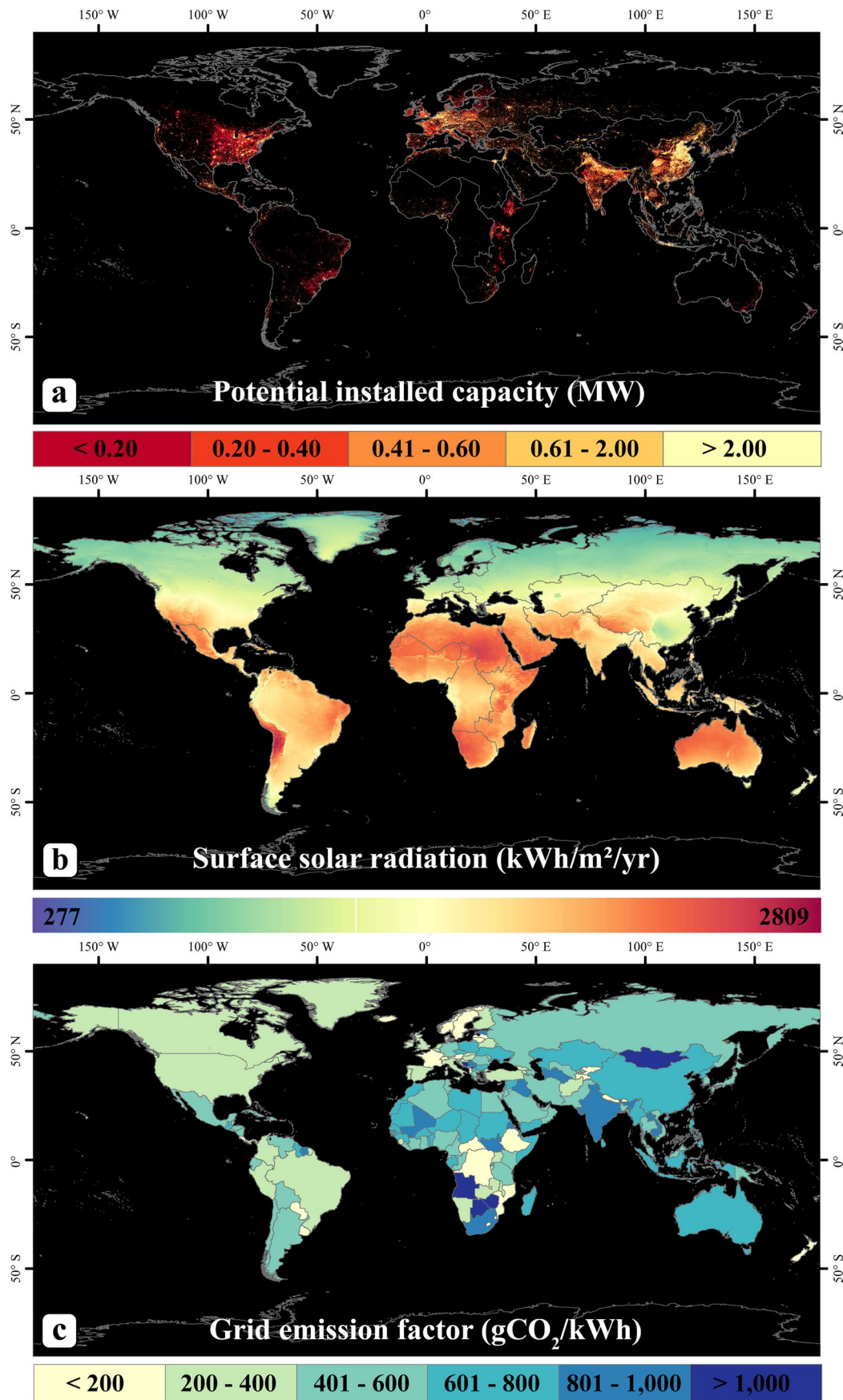


Extended Data Fig. 7 | Analysis of rooftop area distribution. **a**, Overview of global rooftop area distribution (132,799,422 grid samples). **b–u**, Provides detailed breakdown of the rooftop area distributions in specific regions. **b**, Australia and New Zealand (7,931,395 grid samples). **c**, Pacific Islands (535,745 grid samples). **d**, Caribbean (224,661 grid samples). **e**, Northern America (20,876,408 grid samples). **f**, Central America (2,447,734 grid samples). **g**, South America (17,573,960 grid samples). **h**, Eastern Asia (11,563,371 grid samples). **i**, South-Eastern Asia (4,384,788 grid samples). **j**, Southern Asia (6,573,259 grid samples). **k**, Western Asia (4,492,910 grid samples). **l**, Central Asia (3,914,862 grid samples). **m**, Northern Africa (7,604,272 grid samples). **n**, Eastern Africa (6,838,522 grid samples). **o**, Southern Africa (2,662,056 grid samples). **p**, Western Africa (6,030,223 grid samples). **q**, Middle Africa (6,528,310 grid samples). **r**, Northern Europe (1,753,492 grid samples). **s**, Eastern Europe (18,462,618 grid samples). **t**, Southern Europe (1,305,571 grid samples). **u**, Western Europe (1,095,265 grid samples).

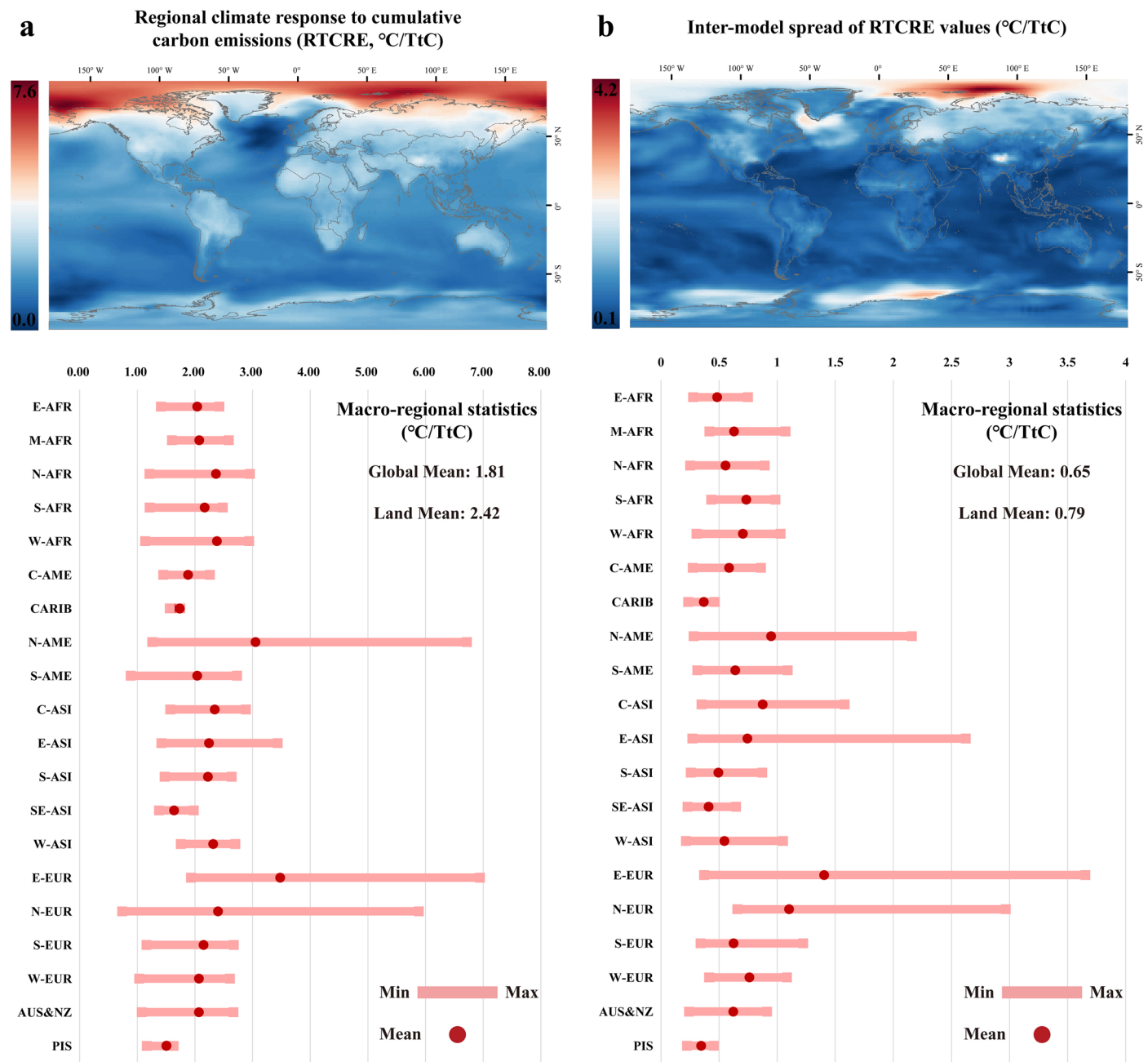


Extended Data Fig. 8 | Quantitative comparison of global rooftop area estimates with reference datasets. **a**, Grid-level comparison with Google Building Footprints (GBF), based on 17,497,097 overlapping grid cells. **b**, Grid-level comparison with Microsoft Building Footprints (MBF), based on 20,303,584 overlapping grid cells. **c**, Grid-level comparison with Global Human Settlement Layer (GHSL), based on 132,799,408 overlapping grid cells. **d**, Grid-level comparison with World Settlement Footprint 3D (WSF3D), based on 24,834,895 overlapping grid cells. Due to the limited coverage and potential spatial

completeness issues in the GBF and MBF datasets, we restricted our comparison to grids that contain building areas in both datasets. For comparisons with GHSL and WSF3D, we used global overlapping grids. The plots show the correlation between our estimated rooftop areas and the corresponding areas from the reference datasets at the grid level. Dashed lines represent the 1:1 relationship. **e**, Grid-level correlation matrix between the different reference datasets and our estimates, highlighting the strong correlations between our global rooftop area estimates and these reference datasets.



Extended Data Fig. 9 | Resource endowment for RPV development. **a.** potential installed capacity, **b.** surface solar radiation, and **c.** grid emission intensity.



Extended Data Fig. 10 | Global distribution of RTCRE. **a.** RTCRE, **b.** intermodal spread.

Reporting Summary

Nature Portfolio wishes to improve the reproducibility of the work that we publish. This form provides structure for consistency and transparency in reporting. For further information on Nature Portfolio policies, see our [Editorial Policies](#) and the [Editorial Policy Checklist](#).

Statistics

For all statistical analyses, confirm that the following items are present in the figure legend, table legend, main text, or Methods section.

n/a Confirmed

- The exact sample size (n) for each experimental group/condition, given as a discrete number and unit of measurement
- A statement on whether measurements were taken from distinct samples or whether the same sample was measured repeatedly
- The statistical test(s) used AND whether they are one- or two-sided
Only common tests should be described solely by name; describe more complex techniques in the Methods section.
- A description of all covariates tested
- A description of any assumptions or corrections, such as tests of normality and adjustment for multiple comparisons
- A full description of the statistical parameters including central tendency (e.g. means) or other basic estimates (e.g. regression coefficient) AND variation (e.g. standard deviation) or associated estimates of uncertainty (e.g. confidence intervals)
- For null hypothesis testing, the test statistic (e.g. F , t , r) with confidence intervals, effect sizes, degrees of freedom and P value noted
Give P values as exact values whenever suitable.
- For Bayesian analysis, information on the choice of priors and Markov chain Monte Carlo settings
- For hierarchical and complex designs, identification of the appropriate level for tests and full reporting of outcomes
- Estimates of effect sizes (e.g. Cohen's d , Pearson's r), indicating how they were calculated

Our web collection on [statistics for biologists](#) contains articles on many of the points above.

Software and code

Policy information about [availability of computer code](#)

Data collection	All spatial datasets used in this study were collected from relevant portals, as shown in data availability and supplementary materials or spatial datasets used in this study were collected from relevant portals, as shown in data availability and supplementary materials.
Data analysis	All processing scripts were developed by ourselves on Python (3.8) and ArcGIS (10.6) were used to process and analyze spatial datasets. The deep learning code was developed using MMSegmentation (0.28).

For manuscripts utilizing custom algorithms or software that are central to the research but not yet described in published literature, software must be made available to editors and reviewers. We strongly encourage code deposition in a community repository (e.g. GitHub). See the Nature Portfolio [guidelines for submitting code & software](#) for further information.

Data

Policy information about [availability of data](#)

All manuscripts must include a [data availability statement](#). This statement should provide the following information, where applicable:

- Accession codes, unique identifiers, or web links for publicly available datasets
- A description of any restrictions on data availability
- For clinical datasets or third party data, please ensure that the statement adheres to our [policy](#)

The estimation results of global rooftop area in our study are available from the corresponding author on reasonable request. Source data are provided in Methods and Supplementary Materials.

Human research participants

Policy information about [studies involving human research participants and Sex and Gender in Research](#).

Reporting on sex and gender	Not relevant to our study. Our study do not involve human research participants and Sex and Gender in Research.
Population characteristics	Not relevant to our study. Our study do not involve human research participants and Sex and Gender in Research.
Recruitment	Not relevant to our study. Our study do not involve human research participants and Sex and Gender in Research.
Ethics oversight	Not relevant to our study. Our study do not involve human research participants and Sex and Gender in Research.

Note that full information on the approval of the study protocol must also be provided in the manuscript.

Field-specific reporting

Please select the one below that is the best fit for your research. If you are not sure, read the appropriate sections before making your selection.

Life sciences Behavioural & social sciences Ecological, evolutionary & environmental sciences

For a reference copy of the document with all sections, see nature.com/documents/nr-reporting-summary-flat.pdf

Behavioural & social sciences study design

All studies must disclose on these points even when the disclosure is negative.

Study description	This study quantified 286,393 km ² of rooftops worldwide through spatial data mining and artificial intelligence. Using the estimated rooftop area and nine advanced Earth System Models from CMIP6, this study revealed that rooftop photovoltaics could substantially contribute to reducing global temperatures by 0.05 - 0.13°C by 2050.
Research sample	This study trained a deep learning model using labelled satellite images, covering 1,600 km ² from various locations worldwide, including 835,253 labelled buildings. This study initially trained it with publicly available benchmark datasets (covering approximately 2,500 km ²) from different satellite sources. 1,724 cities covering 20 million km ² were selected to examine rooftop area and used estimated rooftop area and diverse spatial datasets (including built-up proportion, nighttime light intensity, road length, population, tree-cover proportion, terrain elevation, terrain slope, and geographical grid coordinates) to develop regression models and estimate global rooftop area.
Sampling strategy	This study used a optimized spatial sampling to select cities based on their natural and social characteristics, as well as the spatial locations of cities. The objectives were optimized by simulated annealing algorithm. This method has been developed by existing studies.
Data collection	This study used publicly available satellite imagery datasets targeting building identification to pre-train a deep learning model. These benchmark datasets were generated from distinct institutions between 2013 and 2020, including images from North America, Europe, and East Asia and covering an area of nearly 2,500 km ² . They also vary in spatial resolution, ranging from very fine (0.1 m per pixel) to less detailed (3 m per pixel). This diversity helps our model adapt to different types of images and learn to recognize patterns more effectively. For fine-tuning our deep learning model and identifying building rooftops in global selected regions, this study used high-quality images from 2020 taken by Google Earth. Other geospatial data like road networks, land use and land cover, population statistics, nighttime light imagery, digital elevation models, and annual temperature and precipitation were all from 2020. We employed these datasets for specific analytical purposes. For example, we used road networks to calculate the length of roads worldwide and used land use data to determine the extent of built-up, vegetation-covered, and water-cover areas. This study organized all geospatial data into a spatial grid with a spatial resolution of 1 km. Specific attributes and derived features of these datasets are provided in the supplementary materials.
Timing	The relevant datasets used for global rooftop area estimation are all in 2020. Solar radiation data are averaged from 2010 to 2018. The grid emissions intensity dataset is obtained in 2021 and it is updated at least once every 2 years.
Data exclusions	The discrete spatial grids (each one km ²) were used as the basis for this study. In the process of rooftop examination and developing regression models, this filtered out the grids without missing satellite imagery, resulting in 8.5 million grid samples.
Non-participation	Not relevant to our study.
Randomization	Not relevant to our study.

Reporting for specific materials, systems and methods

We require information from authors about some types of materials, experimental systems and methods used in many studies. Here, indicate whether each material, system or method listed is relevant to your study. If you are not sure if a list item applies to your research, read the appropriate section before selecting a response.

Materials & experimental systems

n/a	Involved in the study
<input checked="" type="checkbox"/>	Antibodies
<input checked="" type="checkbox"/>	Eukaryotic cell lines
<input checked="" type="checkbox"/>	Palaeontology and archaeology
<input checked="" type="checkbox"/>	Animals and other organisms
<input checked="" type="checkbox"/>	Clinical data
<input checked="" type="checkbox"/>	Dual use research of concern

Methods

n/a	Involved in the study
<input checked="" type="checkbox"/>	ChIP-seq
<input checked="" type="checkbox"/>	Flow cytometry
<input checked="" type="checkbox"/>	MRI-based neuroimaging